

High-Pressure Synthesis, Structures, and Properties of Trivalent A-Site-Ordered Quadruple Perovskites $\text{RMn}_7\text{O}_{12}$ ($\text{R} = \text{Sm}, \text{Eu}, \text{Gd}, \text{and Tb}$)

Lei Zhang,^{†,‡} Noriki Terada,[§] Roger D. Johnson,^{§§} Dmitry D. Khalyavin,^{||} Pascal Manuel,^{||}
Yoshio Katsuya,[⊥] Masahiko Tanaka,[⊥] Yoshitaka Matsushita,[§] Kazunari Yamaura,^{†,‡} Alexei
A. Belik^{*,†}

[†]*Research Center for Functional Materials, National Institute for Materials Science (NIMS),
Namiki 1-1, Tsukuba, Ibaraki 305-0044, Japan*

[‡]*Graduate School of Chemical Sciences and Engineering, Hokkaido University, North 10
West 8, Kita-ku, Sapporo, Hokkaido 060-0810, Japan*

[§]*National Institute for Materials Science (NIMS), Sengen 1-2-1, Tsukuba, Ibaraki 305-0047,
Japan*

^{§§}*Department of Physics, University of Oxford, Clarendon Laboratory, Parks Road, Oxford,
OX1 3PU, United Kingdom*

^{||}*ISIS Facility, Rutherford Appleton Laboratory, Chilton, Didcot, OX11 0QX, United
Kingdom*

[⊥]*Synchrotron X-ray Station at SPring-8, NIMS, Kouto 1-1-1, Sayo-cho, Hyogo 679-5148,
Japan*

Abstract

A-site-ordered quadruple perovskites $\text{RMn}_7\text{O}_{12}$ with $\text{R} = \text{Sm}, \text{Eu}, \text{Gd}, \text{and Tb}$ were synthesized at high pressure and high temperature (6 GPa and about 1570 K), and their structural, magnetic, and dielectric properties are reported. They crystallize in space group $I2/m$ at room temperature. All four compounds exhibit a high-temperature phase transition to the cubic $Im-3$ structure at about 664 K (Sm), 663 K (Eu), 657 K (Gd), and 630 K (Tb). They all show one magnetic transition at $T_{\text{N1}} \approx 82\text{-}87$ K at zero magnetic field, but additional magnetic transitions below $T_{\text{N2}} \approx 12$ K were observed in $\text{SmMn}_7\text{O}_{12}$ and $\text{EuMn}_7\text{O}_{12}$ at high magnetic fields. Very weak kink-like dielectric anomalies were observed at T_{N1} in all compounds. We also observed pyroelectric current peaks near 14 K and frequency-dependent sharp steps in dielectric constant (near 18-35 K) - these anomalies are probably caused by dielectric relaxation, and they are not related to any ferroelectric transitions. $\text{TbMn}_7\text{O}_{12}$ shows signs of non-stoichiometry expressed as $(\text{Tb}_{1-x}\text{Mn}_x)\text{Mn}_7\text{O}_{12}$, and these samples exhibit negative magnetization or magnetization reversal effects of an extrinsic origin on zero-field-cooled curves in intermediate temperature ranges. The crystal structures of $\text{SmMn}_7\text{O}_{12}$ and $\text{EuMn}_7\text{O}_{12}$ were refined from neutron powder diffraction data at 100 K, and the crystal structures of $\text{GdMn}_7\text{O}_{12}$ and $(\text{Tb}_{0.88}\text{Mn}_{0.12})\text{Mn}_7\text{O}_{12}$ were studied by synchrotron X-ray powder diffraction at 295 K.

1. Introduction

Manganese compounds are very popular among inorganic and solid-state chemists and physicists because manganese can change its oxidation state from +2 to +7 resulting in very wide ranges of chemical and electronic properties. In the study of perovskites the most important oxidation states are +2, +3, and +4, which are usually present in such oxides. These oxidation states produce a complex interplay among charge, orbital and spin degrees of freedom, and very interesting properties such as colossal magnetoresistance in $\text{La}_{1-x}\text{Sr}_x\text{MnO}_3$ ¹ and spin-induced ferroelectric properties in RMnO_3 and RMn_2O_5 (R = rare-earth elements).^{2,3}

Seemingly simple quasi-binary systems between trivalent rare-earth oxides and a trivalent manganese oxide, $\text{R}_2\text{O}_3\text{-Mn}_2\text{O}_3$, turned out to be quite complex under high-pressure (HP), high-temperature (HT) conditions.⁴⁻⁶ At ambient pressure, only perovskites with a 1:1 ratio between R and Mn can be prepared, and only for R = La-Dy.⁶ RMnO_3 with R = Ho-Lu and Y adopt a hexagonal modification when synthesized at ambient pressure.⁶ The complexity under HP, HT conditions includes the following points. First, the HP, HT synthesis is needed to stabilize RMnO_3 with R = Ho-Lu and Y (in the bulk form) in the perovskite orthorhombic *Pnma* modification.⁶ Second, the HP, HT synthesis can produce the so-called A-site-ordered $\text{AA}'_3\text{B}_4\text{O}_{12}$ quadruple perovskites with a 1:7 ratio and the $\text{RMn}_7\text{O}_{12}$ stoichiometry.⁷⁻¹³ $\text{RMn}_7\text{O}_{12}$ manganites with R = La,⁷⁻¹¹ Pr,¹² Nd,⁷ and Y¹³ have been reported so far. Third, the HP, HT synthesis can result in the partial charge disproportionation of Mn^{3+} and the appearance of Mn^{2+} and Mn^{4+} in HP products. This scheme produces RMn_3O_6 compounds with a 1:3 ratio, belonging to the so-called A-site columnar-ordered $\text{A}_2\text{A}'\text{A}''\text{B}_4\text{O}_{12}$ quadruple perovskites¹⁴ and having the following charge distribution: $[\text{R}^{3+}_2]_{\text{A}}[\text{Mn}^{3+}]_{\text{A}'}[\text{Mn}^{2+}]_{\text{A}''}[\text{Mn}^{3+}_2]_{\text{B1}}[\text{Mn}^{3+}\text{Mn}^{4+}]_{\text{B2}}\text{O}_{12}$.⁴ Partial charge disproportionation can also lead to $(\text{R}_{0.667}\text{Mn}_{0.333})\text{MnO}_3$ compounds with a 1:2 ratio, having the same *Pnma* structure as RMnO_3 and the following charge distribution: $[\text{R}^{3+}_{0.667}\text{Mn}^{2+}_{0.333}]_{\text{A}}[\text{Mn}^{3+}_{0.667}\text{Mn}^{4+}_{0.333}]_{\text{B}}\text{O}_3$.⁵

We have investigated the A-site-ordered quadruple perovskites $\text{RMn}_7\text{O}_{12}$ and found the formation of compounds with $\text{R} = \text{La-Er}$ and Y (at 6 GPa and 1470-1670 K). Based on their different physical properties, these compounds can be approximately separated into four groups: (1) $\text{R} = \text{La, Pr, and Nd}$, (2) $\text{R} = \text{Sm-Tb}$, (3) $\text{R} = \text{Dy}$, and (4) $\text{R} = \text{Ho, Er, and Y}$. $\text{LaMn}_7\text{O}_{12}$ belonging to the first group demonstrates two magnetic spin order transitions at $T_{\text{N}2} = 21 \text{ K}$ and $T_{\text{N}1} = 78 \text{ K}$,⁹ which appear to be second-order, and $\text{LaMn}_7\text{O}_{12}$ shows weak dielectric kinks at $T_{\text{N}1}$. Note that $\text{BiMn}_7\text{O}_{12}$ has also two magnetic transitions with $T_{\text{N}2} = 28 \text{ K}$ and $T_{\text{N}1} = 59 \text{ K}$, but with clear peaks on dielectric constant at both $T_{\text{N}2}$ and $T_{\text{N}1}$.¹⁵ $\text{LaMn}_7\text{O}_{12}$ also shows an orbital order (OO) transition from $Im-3$ to $I2/m$ at 650 K,^{10,11} and it keeps the $I2/m$ symmetry down to the low temperatures.⁹ $\text{YMn}_7\text{O}_{12}$ belonging to the fourth group exhibits one second-order magnetic spin order transition at a higher temperature of $T_{\text{N}} = 108 \text{ K}$ without any dielectric anomalies, and it shows an isostructural transition (from $I2/m$ to $I2/m$) at 200 K,¹³ whose nature is still not known. $\text{DyMn}_7\text{O}_{12}$ shows a strongly first-order transition at $T_{\text{N}1} = 108 \text{ K}$ accompanied by a sharp drop on temperature dependence of dielectric constant, and it shows Dy ordering at $T_{\text{N}2} = 8 \text{ K}$. Note that we found that such compounds with small rare-earth elements ($\text{R} = \text{Tb-Er}$ and Y) have actually $(\text{R}_{1-x}\text{Mn}_x)\text{Mn}_7\text{O}_{12}$ compositions.

This work is focused on the A-site-ordered quadruple perovskites $\text{RMn}_7\text{O}_{12}$ with $\text{R} = \text{Sm, Eu, Gd, and Tb}$ belonging to the second group. This group exhibits a high-temperature phase transition to the cubic $Im-3$ structure at about 664 K (Sm), 663 K (Eu), 657 K (Gd), and 630 K (Tb) and one second-order magnetic transition at $T_{\text{N}1} \approx 82\text{-}87 \text{ K}$ with additional magnetic transitions below $T_{\text{N}2} \approx 12 \text{ K}$ found in $\text{SmMn}_7\text{O}_{12}$ and $\text{EuMn}_7\text{O}_{12}$ at high magnetic fields. We observed very weak kink-like dielectric anomalies at $T_{\text{N}1}$ in all compounds. We also found strong dielectric relaxation near 18-35 K together with pyroelectric current peaks at 14 K, which we assigned to extrinsic effects.

2. Experimental

$\text{RMn}_7\text{O}_{12}$ samples with $\text{R} = \text{Sm, Eu, and Gd}$ were prepared from stoichiometric mixtures of Mn_2O_3 and R_2O_3 (99.9%). Samples with total chemical compositions of $\text{TbMn}_7\text{O}_{12}$,

Tb_{0.9}Mn₇O_{11.85}, and Tb_{0.8}Mn₇O_{11.70} (that is, with the corresponding starting molar ratios of Tb, Mn, and O) were prepared from stoichiometric mixtures of Mn₂O₃, Mn₃O₄ (99.99%), and Tb₄O₇ (99.9%). We emphasize that these compositions are equivalent to TbMn₇O₁₂, (Tb_{0.911}Mn_{0.089})Mn₇O₁₂, and (Tb_{0.821}Mn_{0.179})Mn₇O₁₂, respectively, from the view point of the Tb:Mn:O ratios. Throughout the paper we often use shorter formulae, Tb_{0.9}Mn₇O_{11.85} and Tb_{0.8}Mn₇O_{11.70}, for simplicity. However, (Tb_{1-x}Mn_x)Mn₇O₁₂ is used when needed for discussion. Single-phase Mn₂O₃ was prepared from commercial MnO₂ (99.99%) by heating in air at 923 K for 24 h. The mixtures were placed in Au capsules and treated at 6 GPa and about 1570 K for 2 h (heating time to the synthesis temperature was 10 min) in a belt-type high-pressure apparatus. After the heat treatments, the samples were quenched to room temperature (RT), and the pressure was slowly released. All the samples obtained were black pellets. The temperature of our high-pressure apparatus is controlled by the heating power with a calibrated relationship between power and temperature.

X-ray powder diffraction (XRPD) data were collected at RT on a RIGAKU MiniFlex600 diffractometer using CuK α radiation (2θ range of 8–140°, a step width of 0.02°, and a scan speed of 1 deg/min). High-temperature (HT) XRPD data of GdMn₇O₁₂ were measured on a RIGAKU SmartLab instrument using CuK α_1 radiation (45 kV, 200 mA; 2θ range of 15–105°, a step width of 0.02°, and scan speed of 1 deg/min) from 300 K to 700 K using a furnace attachment. XRPD data were analysed by the Rietveld method using *RIETAN-2000*.¹⁶

Neutron powder diffraction measurements were performed at the ISIS pulsed neutron and muon spallation source at the Rutherford Appleton Laboratory (UK), using the WISH diffractometer located at the second target station.¹⁷ SmMn₇O₁₂ and EuMn₇O₁₂ samples (~1.2 g) were loaded into a cylindrical 3 mm diameter vanadium can and measured at 100 K. Rietveld refinements of the crystal structures were performed using the *FullProf* program¹⁸ against the data measured in detector banks at average 2θ values of 58°, 90°, 122°, and 154°, each covering 32° of the scattering plane. Note that GdMn₇O₁₂ and TbMn₇O₁₂ were not measured because of very strong absorption of neutrons by Gd, and the presence of impurities, respectively.

Synchrotron XRPD data of $\text{GdMn}_7\text{O}_{12}$ and the sample with the total chemical composition of $\text{Tb}_{0.8}\text{Mn}_7\text{O}_{11.70}$ were measured at RT on a large Debye-Scherrer camera at the undulator beamline BL15XU of SPring-8.^{19,20} The intensity data were collected between 3° and 60.34° at 0.003° intervals in 2θ ; the incident beam was monochromatized at $\lambda = 0.65298$ Å. The samples were packed into Lindemann glass capillaries (inner diameter: 0.1 mm), which were rotated during the measurement. The absorption coefficients were also measured. The Rietveld analysis was performed using the *RIETAN-2000* program.¹⁶

Magnetic measurements were performed on SQUID magnetometers (Quantum Design, MPMS-1T and MPMS-XL-7T) between 2 and 350 K (or 400 K) in different applied fields under both zero-field-cooled (ZFC) and field-cooled on cooling (FCC) conditions. Isothermal magnetization measurements were performed between -70 and 70 kOe at different temperatures. Frequency dependent ac susceptibility measurements were performed with a Quantum Design MPMS-1T instrument at different frequencies (f) and different applied oscillating magnetic fields (H_{ac}). Specific heat, C_p , at different magnetic fields (0-90 kOe) was recorded between 2 and 300 K on cooling and heating by a pulse relaxation method using a commercial calorimeter (Quantum Design PPMS). Dielectric properties were measured using a NOVOCONTROL Alpha-A High Performance Frequency Analyzer between 3 and 300 K on cooling and heating in the frequency range of 100 Hz and 2 MHz and at $H = 0$ and 90 kOe. Pyroelectric current measurements were done with a Keithley 6517B electrometer. Poling in different positive and negative electric fields was performed on cooling from 100 K to 5 K at $H = 0$ Oe and 90 kOe; at 5 K, the electric field was removed and electrodes were shorted. Measurements (with a heating rate of 7.5 K/min) were started after the background current was below 1 pA for more than 5 min. Temperature and magnetic fields were controlled by a PPMS. Pieces of pellets were used in all magnetic, specific heat, dielectric, and pyroelectric current measurements.

Differential scanning calorimetry (DSC) curves were recorded on a Mettler Toledo DSC1 STAR^c system at a heating/cooling rate of 10 K/min under N_2 flow between 150 K and 773 K in open Al capsules. Three DSC runs were performed to check the reproducibility.

3. Results and Discussion

3.1. XRPD Studies and Phase Transitions of $\text{RMn}_7\text{O}_{12}$. $\text{SmMn}_7\text{O}_{12}$, $\text{EuMn}_7\text{O}_{12}$, and $\text{GdMn}_7\text{O}_{12}$ samples were almost single-phase with the occasional appearance (for some batches) of traces of Mn_2O_3 impurity. Impurities were below the detection limit on neutron powder diffraction data (for $\text{SmMn}_7\text{O}_{12}$ and $\text{EuMn}_7\text{O}_{12}$). However, $\text{TbMn}_7\text{O}_{12}$ contained about 6 wt. % of TbMn_2O_5 impurity,³ where weight fractions were estimated by *RIETAN-2000* from the refined scale factors in the Rietveld fittings. The appearance of TbMn_2O_5 (instead of TbMn_3O_6 , which is the next phase in the Tb_2O_3 - Mn_2O_3 system)⁴ could be caused by a small non-stoichiometry of the initial chemical Tb_4O_7 because TbMn_2O_5 has an excess of oxygen (or 50 % of Mn^{4+}) in comparison with $\text{TbMn}_7\text{O}_{12}$ (and TbMn_3O_6). The TbMn_2O_5 impurity is Tb-rich; therefore, the main perovskite phase could be Mn-rich. To check this possibility we prepared samples with total chemical compositions of $\text{Tb}_{0.9}\text{Mn}_7\text{O}_{11.85}$ and $\text{Tb}_{0.8}\text{Mn}_7\text{O}_{11.70}$. The amount of the TbMn_2O_5 impurity in $\text{Tb}_{0.9}\text{Mn}_7\text{O}_{11.85}$ was reduced to about 2.2 wt. %, while $\text{Tb}_{0.8}\text{Mn}_7\text{O}_{11.70}$ already contained about 4 wt. % of Mn_2O_3 impurity (that is, the end member of the Tb_2O_3 - Mn_2O_3 system). These facts suggest that chemical compositions of the quadruple perovskite phases should lie between $\text{Tb}_{0.9}\text{Mn}_7\text{O}_{11.85}$ and $\text{Tb}_{0.8}\text{Mn}_7\text{O}_{11.70}$. The structural analysis (see below) showed that the Mn-rich phases should be expressed as $(\text{Tb}_{1-x}\text{Mn}_x)\text{Mn}_7\text{O}_{12}$ with full occupation of all sites. Therefore, the compositions of the quadruple perovskite phases should lie between $(\text{Tb}_{0.91}\text{Mn}_{0.09})\text{Mn}_7\text{O}_{12}$ and $(\text{Tb}_{0.82}\text{Mn}_{0.18})\text{Mn}_7\text{O}_{12}$. XRPD patterns of all compounds are shown on Figure S1 and the lattice parameters are summarized in Table 1. All compounds crystallize in space group $I2/m$ at RT. The lattice parameters of $(\text{Tb}_{1-x}\text{Mn}_x)\text{Mn}_7\text{O}_{12}$ (with the total chemical compositions corresponding to $x = 0$, $x \approx 0.089$, and $x \approx 0.179$) were slightly different and changed monotonically with x ; this fact confirms the formation of a limited range of solid solutions. Ideally, the lattice parameters and magnetic transition temperatures (see below) of perovskite phases in the $\text{TbMn}_7\text{O}_{12}$ and $\text{Tb}_{0.9}\text{Mn}_7\text{O}_{11.85}$ samples should be the same. However, in reality, both cation and oxygen contents of the perovskite phases could slightly vary resulting in different properties.

Figure 1 depicts DSC curves of $\text{RMn}_7\text{O}_{12}$ ($\text{R} = \text{Sm}, \text{Eu}, \text{Gd}, \text{and Tb}$) between 500 and 770 K. Sharp peaks were observed at $T_{\text{OO}} = 664$ K ($\text{R} = \text{Sm}$), 663 K ($\text{R} = \text{Eu}$), and 657 K ($\text{R} = \text{Gd}$) on heating with a hysteresis on cooling indicating structural phase transitions of the first order (Figure S2). The DSC anomalies (at $T_{\text{OO}} = 630$ K) were weaker and much broader in the sample with the total composition of $\text{TbMn}_7\text{O}_{12}$. These features and the drop of T_{OO} could be caused by the fact that the perovskite phase has a $(\text{Tb}_{1-x}\text{Mn}_x)\text{Mn}_7\text{O}_{12}$ composition. The peak positions and areas (about 4.5 J/g for Sm, Eu, and Gd and about 2.5 J/g for Tb) were well reproduced on cycling. No other anomalies were found between 150 and 773 K suggesting the absence of any other structural transitions. The phase transitions at T_{OO} correspond to a transition to the parent cubic structure of the A-site-ordered quadruple perovskites with $Im\bar{3}$ symmetry (Figure S1i). Similar transitions were found in $\text{LaMn}_7\text{O}_{12}$ ($T_{\text{OO}} = 650$ K)¹⁰ and $\text{BiMn}_7\text{O}_{12}$ ($T_{\text{OO}} = 608$ K).²¹ The evolution of HT laboratory XRPD patterns and temperature dependence of the lattice parameters of $\text{GdMn}_7\text{O}_{12}$ are shown on Figures 2 and 3. Note that the a and c parameters are reversed near 530 K. However, this is most probably an artifact. As discussed below, $\text{GdMn}_7\text{O}_{12}$ has almost a pseudo-orthorhombic cell at RT meaning that XRPD patterns can actually be fitted with $a = c$ (Figure 3a and Table S1). But free refinements of a and c produced this reversal. The artifact could originate from the use of the RT atomic coordinates in all refinements and the ability of exchange of a and c parameters in monoclinic cells. Indeed when we first refined atomic coordinates above 530 K with the fixed relation, $a > c$, this relation retained when a and c parameters were further refined.

3.2. Crystal Structures of $\text{RMn}_7\text{O}_{12}$. The structural analysis of the sample with the total chemical composition of $\text{Tb}_{0.8}\text{Mn}_7\text{O}_{11.70}$ showed that the occupation factor (g) of the Tb site was $g(\text{Tb}) = 0.924(19)$, and this value was significantly larger than the expected value of 0.8 for a vacancy model. In addition, all oxygen sites had normal atomic displacement parameters ($B(\text{O}) = 0.2\text{--}0.7 \text{ \AA}^2$). These facts suggested that all sites are fully occupied, and the composition should be written as $(\text{Tb}_{1-x}\text{Mn}_x)\text{Mn}_7\text{O}_{12}$. The composition was refined with a constraint: $g(\text{Tb}) + g(\text{Mn}) = 1$, and the refined value of $g(\text{Tb}) = 0.883(3)$ lies between 0.82 and 0.91. [The refinement of $g(\text{Tb})$ was performed together with all other refined

parameters.] The crystal structure parameters of $(\text{Tb}_{0.88}\text{Mn}_{0.12})\text{Mn}_7\text{O}_{12}$ are summarized in Table 2, and Figure 4 shows the fitting results. Note that the composition was calculated to be $(\text{Tb}_{0.86}\text{Mn}_{0.14})\text{Mn}_7\text{O}_{12}$ taking into account the presence of 3.9 wt. % of Mn_2O_3 impurity in the sample with the total chemical composition of $\text{Tb}_{0.8}\text{Mn}_7\text{O}_{11.70}$ (Figure S3); and the calculated composition is close to the refined composition. The formation of $(\text{Tb}_{1-x}\text{Mn}_x)\text{Mn}_7\text{O}_{12}$ with full occupation of all sites instead of $\text{Tb}_{1-y}\text{Mn}_7\text{O}_{12-1.5y}$ with vacancies under HP, HT conditions could be explained by a larger density of the former. However, we emphasize that the appearance of a small level of oxygen non-stoichiometry, $(\text{Tb}_{1-x}\text{Mn}_x)\text{Mn}_7\text{O}_{12\pm\delta}$, cannot be excluded.

Mn at large A sites of perovskites usually has the +2 oxidation state.⁵ Therefore, we can assume the +2 oxidation state of Mn at the A site of $(\text{Tb}_{1-x}\text{Mn}_x)\text{Mn}_7\text{O}_{12}$. The charge compensation can be achieved by three ways (or even by their combinations): first, through oxygen vacancies; second, through the formation of a small amount of Tb^{4+} at the A site; third, through the formation of a small amount of Mn^{4+} at the B sites. However, the size of Tb^{4+} ($r_{\text{VIII}} = 0.88 \text{ \AA}$)²² is much smaller than that of Tb^{3+} ($r_{\text{VIII}} = 1.040 \text{ \AA}$), and the formation of Tb^{4+} at a large A site would be unfavourable. Moreover, our neutron diffraction studies of $(\text{Y}_{0.8}\text{Mn}_{0.2})\text{Mn}_7\text{O}_{12}$ (with a stable oxidation state of +3 for Y) showed no oxygen vacancies within the accuracy of the method. Therefore, we suggest that the charge compensation is realized through the formation of a small amount of Mn^{4+} at the B sites in all non-stoichiometric $(\text{R}_{1-x}\text{Mn}_x)\text{Mn}_7\text{O}_{12}$ compounds.

The refined a and c lattice parameters of $(\text{Tb}_{0.88}\text{Mn}_{0.12})\text{Mn}_7\text{O}_{12}$ were slightly different, but the difference was very small, and no reflection splitting was actually observed (even on high resolution synchrotron XRPD data and in high 2θ regions (Figure S1d and S1e)). It means that the monoclinic $I2/m$ cell could be transformed to an orthorhombic cell ($\mathbf{a}_O = \mathbf{a}_M + \mathbf{c}_M$, $\mathbf{b}_O = \mathbf{b}_M$, and $\mathbf{c}_O = \mathbf{a}_M - \mathbf{c}_M$). Synchrotron XRPD data could be well fitted in space group $Fmmm$ by the Rietveld method (with $a = 10.42828(2) \text{ \AA}$, $b = 7.34693(1) \text{ \AA}$, and $c = 10.62318(2) \text{ \AA}$) with almost the same R values (Table S2). However, a $Fmmm$ structural model had unrealistic disordering of the oxygen sublattice, and $Fmmm$ is not a subgroup of the parent $Im\bar{3}$ structure.²¹ Therefore, the real symmetry should be $I2/m$.²¹ The origin of pseudo-orthorhombic metrics remains unclear. Pseudo-orthorhombic metrics were also

observed in $\text{BiMn}_7\text{O}_{12}$ (between 460 and 608 K),²¹ $\text{YMn}_7\text{O}_{12}$ (above 200 K),¹³ and $(\text{R}_{1-x}\text{Mn}_x)\text{Mn}_7\text{O}_{12}$ (with R = Dy, Ho, Er, and Y for $x \approx 0.2$ and at RT). We note that reflection splitting corresponding to the difference between the a and c monoclinic lattice parameters was clearly observed in $\text{SmMn}_7\text{O}_{12}$ and $\text{EuMn}_7\text{O}_{12}$, but $\text{GdMn}_7\text{O}_{12}$ was almost pseudo-orthorhombic (Figure S1f).

The crystal structure parameters of $\text{SmMn}_7\text{O}_{12}$ and $\text{EuMn}_7\text{O}_{12}$ from neutron powder diffraction data at 100 K are summarized in Table 3, and bond lengths, Mn-O-Mn bond angles, bond valence sums (BVS),²³ and distortion parameters of MnO_6 octahedra in Table 4. Note that atomic displacement parameters have not been given as these could not be reliably refined in the presence of strong absorption by the rare earth elements. Figure 5 shows the fitting results for $\text{SmMn}_7\text{O}_{12}$ and $\text{EuMn}_7\text{O}_{12}$.

The crystal structure parameters of $\text{GdMn}_7\text{O}_{12}$ from synchrotron XRPD data are given in Tables S3 and S4, and fitting results are shown on Figures S1g and S1h.

$\text{SmMn}_7\text{O}_{12}$ and $\text{EuMn}_7\text{O}_{12}$ have the same structural features as $\text{LaMn}_7\text{O}_{12}$,⁹ $\text{PrMn}_7\text{O}_{12}$,¹² and $\text{YMn}_7\text{O}_{12}$.¹³ They have MnO_6 octahedra that are strongly distorted by the cooperative Jahn-Teller effect. The distortion has a very common Q_2 mode, that is, two opposite oxygen atoms move closer to Mn, two opposite oxygen atoms move far from Mn, and two opposite oxygen atoms stay at almost the same distance to Mn in comparison with an undistorted MnO_6 octahedron. The octahedral distortion parameter, $\Delta(\text{Mn})$, is about 1.9×10^{-3} for the Mn4 and Mn5 sites in both compounds. The BVS values of the Mn4 and Mn5 octahedral sites were slightly larger than expected (+3.2-3.3), but the same tendency was also observed in $\text{LaMn}_7\text{O}_{12}$ (+3.22 and +3.18),⁹ $\text{PrMn}_7\text{O}_{12}$ (+3.23 and +3.25),¹² and $\text{YMn}_7\text{O}_{12}$ (+3.2 and +3.4).¹³ The BVS values of the Mn1, Mn2, and Mn3 square-planar coordinated sites were slightly smaller than expected (+2.7-2.9), but again the same tendency was observed in $\text{LaMn}_7\text{O}_{12}$ (+2.8-3.0)⁹ and $\text{YMn}_7\text{O}_{12}$ (+2.7-2.8 for two sites).¹³ These features, which were also observed in $\text{AMn}_7\text{O}_{12}$ (A = Cd, Ca, Sr, and Pb),^{24,25} could be caused by specific coordination environments of the corresponding sites.

Most of the Mn-O and R-O bond lengths of $(\text{Tb}_{0.88}\text{Mn}_{0.12})\text{Mn}_7\text{O}_{12}$ are very similar with the corresponding values of $\text{SmMn}_7\text{O}_{12}$ and $\text{EuMn}_7\text{O}_{12}$. This fact gives indirect evidence that the charge distribution should be very similar in these compounds. In other words, Tb should

adopt the oxidation state of +3, and not +4. Ce has a stronger tendency to adopt the +4 oxidation state than Tb; however, we found that $\text{CeMn}_7\text{O}_{12}$ and $\text{CeCuMn}_6\text{O}_{12}$ are formed with the +3 oxidation state for Ce.²⁶ The lattice parameters (a , b , and c) and unit cell volume of $\text{TbMn}_7\text{O}_{12}$ have no anomalies in the $\text{RMn}_7\text{O}_{12}$ series, while the presence of cations in different oxidation states at the A site results in lattice anomalies.²⁷ The oxidation state of Tb was also suggested to be +3 in $\text{TbCu}_3\text{Mn}_4\text{O}_{12}$.²⁸ Therefore, we have a lot of indirect evidence from the crystallographic considerations that the oxidation state of Tb is +3.

The BVS values of the R sites are lower than +3, and the BVS value decreases with decreasing the size of R (Table 4 and BVS = +2.37 in $\text{YMn}_7\text{O}_{12}$).¹³ This feature is caused by strong and almost fixed tilts of the MnO_6 framework, which creates almost constant-size cavities.¹⁴ Large mismatch between the size of the cavity and the size of the rare-earth elements could be a reason for the cation non-stoichiometry of $(\text{R}_{1-x}\text{Mn}_x)\text{Mn}_7\text{O}_{12}$ with small rare-earth elements.

3.3. Magnetic and Dielectric Properties of $\text{RMn}_7\text{O}_{12}$. Figures 6 and 7 (and Figures S4-S8) depict dc magnetic susceptibilities of $\text{RMn}_7\text{O}_{12}$. These data show one magnetic transition at $T_{\text{N1}} = 87$, 87, 86, and 82 K for R = Sm, Eu, Gd, and Tb, respectively, where T_{N1} is determined from peak positions on the FCC $d\chi T/dT$ vs T curves measured at 100 Oe. T_{N1} is almost the same for R = Sm, Eu, and Gd, while it drops for R = Tb. This fact could be explained by a small deviation of the stoichiometry of the perovskite phase from the ideal $\text{TbMn}_7\text{O}_{12}$. This is further confirmed by the drop of T_{N1} to 75 K in $\text{Tb}_{0.8}\text{Mn}_7\text{O}_{11.70}$ (Figures S7 and S8). At 100 Oe, ZFC and FCC χ vs T curves exhibit strong divergence below T_{N1} that is typical for ferrimagnets and canted antiferromagnets. At 10 kOe, ZFC and FCC χ vs T curves almost coincide with each other and show small divergence at low temperatures. At high magnetic fields, additional magnetic anomalies appear in $\text{SmMn}_7\text{O}_{12}$ and $\text{EuMn}_7\text{O}_{12}$ (insets of Figure 6). In $\text{EuMn}_7\text{O}_{12}$, additional upturns are observed from 8 K at 10 kOe (Figures S5) and from 13 K at 70 kOe. In $\text{SmMn}_7\text{O}_{12}$ an upturn appears from 8 K at 70 kOe (Figure 6), accompanied by broad maxima near 20 K (at 10 kOe) and 23 K (at 70 kOe). $\text{LaMn}_7\text{O}_{12}$ ($T_{\text{N2}} = 23$ K and $T_{\text{N1}} = 79$ K), $\text{PrMn}_7\text{O}_{12}$ ($T_{\text{N2}} = 13$ K and $T_{\text{N1}} = 83$ K), and $\text{NdMn}_7\text{O}_{12}$ ($T_{\text{N2}} = 13$ K and $T_{\text{N1}} = 85$ K; our own data for all compounds) have two magnetic

transitions at zero magnetic field, where the transition at T_{N2} is related to Mn at the A' sites.⁹ Therefore, transitions near $T_{N2} \approx 12$ K at high magnetic fields in compounds with the next rare-earth elements ($R = \text{Sm}$ and Eu) could also be caused by Mn at the A' sites. Neutron diffraction experiments under magnetic fields are needed to confirm this suggestion. We note that the involvement of the rare-earth sublattice is unlikely because of almost non-magnetic nature of Eu^{3+} and Sm^{3+} cations.²⁹ We are not aware of any simple RMO_3 perovskites (e.g., $M = \text{Cr}$, Mn , and Fe) with a long-range order of Eu^{3+} and Sm^{3+} cations, while most of other (magnetic) rare-earth cations show long-range order.³⁰

$\text{TbMn}_7\text{O}_{12}$, $\text{Tb}_{0.9}\text{Mn}_7\text{O}_{11.85}$, and $\text{Tb}_{0.8}\text{Mn}_7\text{O}_{11.70}$ samples exhibit negative magnetization or magnetization reversal effects on ZFC curves in intermediate temperature ranges (the inset of Figure 7b). Because these effects have attracted a lot of attention recently^{31,32} we performed more detailed measurements on $\text{Tb}_{0.9}\text{Mn}_7\text{O}_{11.85}$ (Figure 8) and will discuss the origin of these effects in this paragraph. First, we emphasize that trapped fields inside magnetometers were always positive (PTF: positive trapped field) for these measurements as confirmed by a superconducting sample.³³ Zero PTF means a field below about 0.01 Oe,³³ but we also intentionally set PTF of 3 Oe in some cases. Negative magnetization was only observed during the so-called quenched zero-field-cooled (q-ZFC) procedure, when a sample was rapidly (within 2-5 min) inserted into a magnetometer, which was kept at 10 K; after inserting a sample, temperature was set to 2 K; and finally at 2 K, a measurement magnetic field was applied (in this work, $\text{ZFC} \equiv \text{q-ZFC}$). After inserting a sample at nominally zero field, magnetization was negative (Figure 8). It means that a preferred domain structure was built with negative magnetization even in PTF during the sample movement. The application of a measurement magnetic field of 100 Oe at 2 K could initially reverse negative magnetization to a positive value for some reasons even though the coercive field is much larger than 100 Oe (see below). Specific temperature evolution of the established domain structure with negative magnetization could win again in intermediate temperature ranges. No negative magnetization was observed during the so-called slow zero-field-cooled (s-ZFC) procedure, when a sample was inserted into a magnetometer at 300 K; after inserting a sample, temperature was (very slowly) set to 2 K; and finally at 2 K, a measurement magnetic field was applied. These results demonstrate an extrinsic origin of the observed

negative magnetization and show that the sample insertion procedure also plays an important role in addition to the sign of the trapped fields.³² The effect of the sample insertion procedure on ZFC curves was also observed in $\text{YVO}_{3+\delta}$ ³³ and $\text{BiMnO}_3\text{-BiCrO}_3$ solid solutions.³⁴

Ac susceptibility measurements (Figures S9-S14) show frequency-independent sharp peaks on both χ' vs T and χ'' vs T curves at T_{N1} that is typical for ferrimagnets and canted antiferromagnets. Peak intensities on the χ' vs T and χ'' vs T curves depend on the H_{ac} field due to interactions of the H_{ac} field with magnetic domain structures.

Specific heat measurements (Figures 9 and 10) confirm the presence of one magnetic transition at T_{N1} . No hysteresis was observed on cooling and heating suggesting a magnetic phase transition of the second order. Specific heat measurements of $\text{SmMn}_7\text{O}_{12}$ and $\text{EuMn}_7\text{O}_{12}$ at high magnetic fields show the emergence of weak anomalies below $T_{N2} \approx 12$ K (insets of Figure 9 and Figures S15 and S16), confirming the appearance of new field-induced magnetic transitions. The C_p/T vs T curves of $\text{GdMn}_7\text{O}_{12}$ at $H = 0$ Oe demonstrate a gradual rise below 10 K; this feature could be caused by Schottky-like or short-range contributions from Gd^{3+} cations; and this rise is suppressed by magnetic fields (the inset of Figure 10a and Figure S17).

The inverse magnetic susceptibilities follow the Curie-Weiss law. Between 200 and 395 K, the inverse magnetic susceptibilities (measured at 70 kOe in the FCC mode) are fit by the Curie-Weiss equation (Figure S18)

$$\chi(T) = \mu_{\text{eff}}^2 N (3k_B(T - \theta))^{-1} \quad (1)$$

where μ_{eff} is an effective magnetic moment, N is Avogadro's number, k_B is Boltzmann's constant, and θ is the Curie-Weiss temperature. The fitting parameters are summarized in Table 5. The μ_{eff} values are in good agreement with the theoretical values, where μ_{calc} is calculated using typical values for rare-earth cations: $1.5\mu_B$ for Sm^{3+} , $3.4\mu_B$ for Eu^{3+} , $8\mu_B$ for Gd^{3+} , and $9.5\mu_B$ for Tb^{3+} .²⁹ The negative Curie-Weiss temperatures show that the strongest exchange interactions are antiferromagnetic in nature.

Figures 11 and S19 demonstrates M vs H curves at 5 K; the parameters are summarized in Table 5. All samples show clear hysteresis typical for ferrimagnets and canted

antiferromagnets. However, the remnant magnetisation values are quite large for canted antiferromagnets. Therefore, ferrimagnetic models are more probable. Further neutron diffraction studies are needed for the determination of magnetic structures, which will be reported elsewhere.

Figure 12 shows dielectric data for $\text{SmMn}_7\text{O}_{12}$ as an example (other samples have very similar dielectric properties (Figures S20-S25); and we also observed similar dielectric behavior in $\text{LaMn}_7\text{O}_{12}$, $\text{PrMn}_7\text{O}_{12}$, and $\text{NdMn}_7\text{O}_{12}$ belonging to the first group and in $\text{CeMn}_7\text{O}_{12}$, but not in $(\text{R}_{1-x}\text{Mn}_x)\text{Mn}_7\text{O}_{12}$ with $\text{R} = \text{Dy}, \text{Ho}, \text{Er}, \text{and Y}$ belonging to the third and fourth groups). First, we observe small kinks at T_{N1} at high frequencies; at low frequencies, these kinks are probably hidden by a rapid increase of dielectric constant due to extrinsic effects (such as increased conductivity). Second, we observe sharp drops near 18-35 K, where the exact temperature is strongly frequency-dependent. At the same time, sharp peaks (at T_{max}) are observed in the dielectric loss measured as a function of temperature, which shows a similar frequency-dependence. T_{max} is about 15 K if extrapolated to low frequencies (the inset of Figure 12a), and it is close to an observed pyroelectric current peak (see the next paragraph). Such a dependence on frequency gives strong evidence that these anomalies are not intrinsic, but that they are caused by dielectric relaxation processes. No hysteresis was observed between cooling and heating curves (Figure 13). A magnetic field of 90 kOe slightly shifts the dielectric kink at T_{N1} to higher temperature (Figure 13) in agreement with specific heat results. From the dielectric data at $H = 0$ and 90 kOe, the magnetodielectric effect is found to be negligible in these $\text{RMn}_7\text{O}_{12}$ compounds (see also Figures S26 and S27). Note that dielectric properties of $\text{TbMn}_7\text{O}_{12}$ were strongly affected by the presence of TbMn_2O_5 impurity (Figure 13d).³

Pyroelectric current measurements demonstrate peaks near 14 K and very broad peaks near 90 K (Figure 14). Very similar broad peaks near 80-90 K were also observed in divalent A-site-ordered quadruple perovskites $\text{AMn}_7\text{O}_{12}$ ($\text{A} = \text{Cd}, \text{Ca}, \text{Sr}, \text{and Pb}$) and assigned to thermally stimulated current.^{24,35,36} The peaks near 90 K in $\text{RMn}_7\text{O}_{12}$ are also caused by thermally stimulated current.³⁶ Therefore, we will focus our discussion on the peaks near 14 K. At first glance, these peaks look intrinsic for some compounds as their polarity reverses when the poling electric field changes sign (Figure 14b), and we obtain a maximum

‘polarization’ of $3 \mu\text{C}/\text{m}^2$ in $\text{SmMn}_7\text{O}_{12}$ (Figure S28) when integrated. However, the pyroelectric current peaks were quite symmetrical, while (ideally) sharp drops of pyroelectric current would be expected above T_C for a ferroelectric phase transition.^{37,38} Secondly, measurements by the bias electric field method gave positive (or up) peaks near 14 K (Figure 15), while negative (or down) peaks would be expected for a ferroelectric phase transition.³⁶⁻³⁸ Finally, a transition around 14 K was not detectable by other methods. The reversibility of pyroelectric current with the change of the sign of a poling field was not observed in case of $\text{EuMn}_7\text{O}_{12}$ (Figures 14c and 14d), and the different behavior of pyroelectric current in $\text{SmMn}_7\text{O}_{12}$ and $\text{EuMn}_7\text{O}_{12}$ upon reversal of the poling field is not clear. We note that very similar pyroelectric current peaks near 14 K were also observed by us in $\text{LaMn}_7\text{O}_{12}$ and $\text{CeMn}_7\text{O}_{12}$. All these facts coupled with the observation of strong dielectric relaxation (Figure 12) allow us to conclude that the observed dielectric and pyroelectric current anomalies are not caused by any ferroelectric polarization. The accumulation of information on all members of the $\text{RMn}_7\text{O}_{12}$ family (Figures 13 and 14) and the comparative analysis were very important for the correct interpretation of dielectric and pyroelectric current results. We emphasize that the reversibility of pyroelectric current with the change of the sign of a poling field is a necessary but not sufficient condition to prove the ferroelectric nature of transitions, and very broad and symmetrical pyroelectric current peaks are strong indicators of their non-ferroelectric nature (even in the vicinity of magnetic transitions).

4. Conclusion

We clarified the structural and physical properties of a group of A-site-ordered quadruple perovskites $\text{RMn}_7\text{O}_{12}$ with $\text{R} = \text{Sm}, \text{Eu}, \text{Gd}, \text{and Tb}$. These compounds crystallize in space group $I2/m$ at room temperature, and they show one structural transition to the parent cubic $Im-3$ structure at about 664 K (Sm), 663 K (Eu), 657 K (Gd), and 630 K (Tb). This group of $\text{RMn}_7\text{O}_{12}$ compounds has only one magnetic transition at $T_{N1} \approx 82\text{-}87$ K at zero magnetic field, however, an additional magnetic transition below $T_{N2} \approx 12$ K was observed in $\text{SmMn}_7\text{O}_{12}$ and $\text{EuMn}_7\text{O}_{12}$ at high magnetic fields. They show weak kink-like anomalies on dielectric constant at T_{N1} . We also observed dielectric and pyroelectric current anomalies

near 14-35 K, which were attributed to dielectric relaxation, and not to any ferroelectric transitions. These conclusions are methodologically important from the viewpoint of correctness in the interpretation of pyroelectric current results.

Associated Content

Supporting information

Details of synchrotron and laboratory XRPD patterns, magnetic, and dielectric properties (PDF).

Accession Codes

CCDC 1825014-1825017 contain the supplementary crystallographic data for this paper. These data can be obtained free of charge via www.ccdc.cam.ac.uk/data_request/cif, or by emailing data_request@ccdc.cam.ac.uk, or by contacting The Cambridge Crystallographic Data Centre, 12 Union Road, Cambridge CB21EZ, UK; fax: +44 1223 336033.

Author Information

Corresponding Author

Alexei.Belik@nims.go.jp

Notes

The authors declare no competing financial interest.

Acknowledgements. This work was supported by JSPS KAKENHI Grant Numbers JP15K14133 and JP16H04501 and JSPS Bilateral Open Partnership Joint Research Projects. RDJ acknowledges support from a Royal Society University Research Fellowship. D.D.K and P.M. acknowledge TUMOCs project. This project has received funding from the European Union's Horizon 2020 research and innovation programme under the Marie Skłodowska-Curie Grant Agreements No. 645660. The synchrotron radiation experiments were performed at the SPring-8 with the approval of NIMS Synchrotron X-ray Station (Proposal Number: 2016B4504).

References

- (1) Salamon, M. B.; Jaime, M. The Physics of Manganites: Structure and Transport. *Rev. Mod. Phys.* **2001**, *73*, 583-628.
- (2) Kimura, T.; Goto, T.; Shintani, H.; Ishizaka, K.; Arima, T.; Tokura, Y. Magnetic Control of Ferroelectric Polarization. *Nature (London)* **2003**, *426*, 55-58.
- (3) Hur, N.; Park, S.; Sharma, P. A.; Ahn, J. S.; Guha, S.; Cheong, S. W. Electric Polarization Reversal and Memory in a Multiferroic Material Induced by Magnetic Fields. *Nature (London)* **2004**, *429*, 392-395.
- (4) Zhang, L.; Matsushita, Y.; Yamaura, K.; Belik, A. A. Five-Fold Ordering in High-Pressure Perovskites RMn_3O_6 ($\text{R} = \text{Gd-Tm}$ and Y). *Inorg. Chem.* **2017**, *56*, 5210-5218.
- (5) Zhang, L.; Gerlach, D.; Dönni, A.; Chikyow, T.; Katsuya, Y.; Tanaka, M.; Ueda, S.; Yamaura K.; Belik, A. A. Mn Self-Doping of Orthorhombic RMnO_3 Perovskites: $(\text{R}_{0.667}\text{Mn}_{0.333})\text{MnO}_3$ with $\text{R} = \text{Er-Lu}$. *Inorg. Chem.* **2018**, *57*, 2773-2781.
- (6) Uusi-Esko, K.; Malm, J.; Imamura, N.; Yamauchi, H.; Karppinen, M. Characterization of RMnO_3 ($\text{R} = \text{Sc, Y, Dy-Lu}$): High-Pressure Synthesized Metastable Perovskites and Their Hexagonal Precursor Phases. *Mater. Chem. Phys.* **2008**, *112*, 1029-1034.
- (7) Bochu, B.; Chenavas, J.; Joubert, J. C.; Marezio, M. High Pressure Synthesis and Crystal Structure of a New Series of Perovskite-Like Compounds $\text{CMn}_7\text{O}_{12}$ ($\text{C} = \text{Na, Ca, Cd, Sr, La, Nd}$). *J. Solid State Chem.* **1974**, *11*, 88-93.
- (8) Prodi, A.; Allodi, G.; Gilioli, E.; Licci, F.; Marezio, M.; Bolzoni, F.; Gauzzi, A.; De Renzi, R. μSR Study of $\text{AA}'_3\text{Mn}_4\text{O}_{12}$ Double Perovskites. *Phys. B* **2006**, *374-375*, 55-58.
- (9) Prodi, A.; Gilioli, E.; Cabassi, R.; Bolzoni, F.; Licci, F.; Huang, Q.; Lynn, J. W.; Affronte, M.; Gauzzi, A.; Marezio, M. Magnetic Structure of the High-Density Single-Valent e_g Jahn-Teller System $\text{LaMn}_7\text{O}_{12}$. *Phys. Rev. B: Condens. Matter Mater. Phys.* **2009**, *79*, 085105.
- (10) Okamoto, H.; Karppinen, M.; Yamauchi, H.; Fjellvag, H. High-temperature Synchrotron X-ray Diffraction Study of $\text{LaMn}_7\text{O}_{12}$. *Solid State Sci.* **2009**, *11*, 1211-1215.
- (11) Cabassi, R.; Bolzoni, F.; Gilioli, E.; Bissoli, F.; Prodi, A.; Gauzzi, A. Jahn-Teller-induced Crossover of the Paramagnetic Response in the Singly Valent e_g System $\text{LaMn}_7\text{O}_{12}$. *Phys. Rev. B: Condens. Matter Mater. Phys.* **2010**, *81*, 214412.
- (12) Mezzadri, F.; Calicchio, M.; Gilioli, E.; Cabassi, R.; Bolzoni, F.; Calestani, G.; Bissoli, F. High-Pressure Synthesis and Characterization of $\text{PrMn}_7\text{O}_{12}$ Polymorphs. *Phys. Rev. B: Condens. Matter Mater. Phys.* **2009**, *79*, 014420.
- (13) Verseils, M.; Mezzadri, F.; Delmonte, D.; Baptiste, B.; Klein, Y.; Shcheka, S.; Chapon, L. C.; Hansen, T.; Gilioli, E.; Gauzzi, A. Effect of Chemical Pressure Induced by $\text{La}^{3+}/\text{Y}^{3+}$ Substitution on the Magnetic Ordering of $(\text{AMn}_3)\text{Mn}_4\text{O}_{12}$ Quadruple Perovskites. *Phys. Rev. Mater.* **2017**, *1*, 064407.
- (14) Belik, A. A. Rise of A-site Columnar-ordered $\text{A}_2\text{A}'\text{A}''\text{B}_4\text{O}_{12}$ Quadruple Perovskites with Intrinsic Triple Order. *Dalton Trans.* **2018**, *47*, 3209-3217.

- (15) Imamura, N.; Karppinen, M.; Motohashi, T.; Fu, D.; Itoh, M.; Yamauchi, H. Positive and Negative Magnetodielectric Effects in A-Site Ordered (BiMn₃)Mn₄O₁₂ Perovskite. *J. Am. Chem. Soc.* **2008**, *130*, 14948-14949.
- (16) Izumi, F.; Ikeda, T. A Rietveld-Analysis Program RIETAN-98 and its Applications to Zeolites. *Mater. Sci. Forum* **2000**, *321-324*, 198-205.
- (17) Chapon, L. C.; Manuel, P.; Radaelli, P. G.; Benson, C.; Perrott, L.; Ansell, S.; Rhodes, N. J.; Raspino, D.; Duxbury, D.; Spill, E.; Norris, J. Wish: the New Powder and Single Crystal Magnetic Diffractometer on the Second Target Station. *Neutron News* **2011**, *22*, 22-25.
- (18) Rodriguez, C. J. Recent Advances in Magnetic Structure Determination by Neutron Powder Diffraction. *Phys. B* **1993**, *193*, 55-69.
- (19) Tanaka, M.; Katsuya, Y.; Yamamoto, A. A New Large Radius Imaging Plate Camera for High-Resolution and High-Throughput Synchrotron X-Ray Powder Diffraction by Multiexposure Method. *Rev. Sci. Instrum.* **2008**, *79*, 075106.
- (20) Tanaka, M.; Katsuya, Y.; Matsushita, Y.; Sakata, O. Development of a Synchrotron Powder Diffractometer with a One-Dimensional X-Ray Detector for Analysis of Advanced Materials. *J. Ceram. Soc. Jpn.* **2013**, *121*, 287-290.
- (21) Belik, A. A.; Matsushita, Y.; Kumagai, Y.; Katsuya, Y.; Tanaka, M.; Stefanovich, S. Yu.; Lazoryak, B. I.; Oba F.; Yamaura, K. Complex Structural Behavior of BiMn₇O₁₂ Quadruple Perovskite. *Inorg. Chem.* **2017**, *56*, 12272–12281.
- (22) Shannon, R. D. Revised Effective Ionic Radii and Systematic Studies of Interatomic Distances in Halides and Chalcogenides. *Acta Crystallogr., Sect. A: Cryst. Phys., Diff., Theor. Gen. Crystallogr.* **1976**, *32*, 751–767.
- (23) Brese, N. E.; O’Keeffe, M. Bond-Valence Parameters for Solids. *Acta Crystallogr., Sect. B: Struct. Sci.* **1991**, *47*, 192-197.
- (24) Glazkova, Y. S.; Terada, N.; Matsushita, Y.; Katsuya, Y.; Tanaka, M.; Sobolev, A. V.; Presniakov, I. A.; Belik, A. A. High-Pressure Synthesis, Crystal Structures, and Properties of CdMn₇O₁₂ and SrMn₇O₁₂ Perovskites. *Inorg. Chem.* **2015**, *54*, 9081-9091.
- (25) Belik, A. A.; Glazkova, Y. S.; Katsuya, Y.; Tanaka, M.; Sobolev, A. V.; Presniakov, I. A. Low-Temperature Structural Modulations in CdMn₇O₁₂, CaMn₇O₁₂, SrMn₇O₁₂, and PbMn₇O₁₂ Perovskites Studied by Synchrotron X-ray Powder Diffraction and Mossbauer Spectroscopy. *J. Phys. Chem. C* **2016**, *120*, 8278–8288.
- (26) Zhang, L.; Matsushita, Y.; Katsuya, Y.; Tanaka, M.; Yamaura, K.; Belik, A. A. Charge and Orbital Orders and Structural Instability in High-pressure Quadruple Perovskite CeCuMn₆O₁₂. *J. Phys.: Condens. Matter* **2018**, *30*, 074003.
- (27) Sanchez-Benitez, J.; Alonso, J. A.; Martinez-Lope, M. J.; de Andres A.; Fernandez-Diaz, M. T. Enhancement of the Curie Temperature along the Perovskite Series RCu₃Mn₄O₁₂ Driven by Chemical Pressure of R³⁺ Cations (R = Rare Earths). *Inorg. Chem.* **2010**, *49*, 5679–5685.
- (28) Sanchez-Benitez, J.; Alonso, J. A.; de Andres, A.; Martinez-Lope, M. J.; Martinez, J. L.; Munoz, A. Peculiar Magnetic Behavior of the TbCu₃Mn₄O₁₂ Complex Perovskite. *Chem. Mater.* **2005**, *17*, 5070-5076.
- (29) Kittel, C. *Introduction to Solid State Physics*; 8th Ed., John Wiley and Sons, Inc: New York, 2005.

- (30) Bousquet E.; Cano, A. Non-collinear Magnetism in Multiferroic Perovskites. *J. Phys.: Condens. Matter* **2016**, 28, 123001.
- (31) Kumar, A.; Yusuf, S. M. The Phenomenon of Negative Magnetization and its Implications. *Phys. Rep.* **2015**, 556, 1-34.
- (32) Xie, X. N.; Che, H. L.; Wang, H.; Lin, G. K.; Zhu, H. Negative Zero-Field-Cooled Magnetization in $\text{YMn}_{0.5}\text{Cr}_{0.5}\text{O}_3$ Due to Giant Coercivity and Trapped Field. *Inorg. Chem.* **2018**, 57, 175-180.
- (33) Belik, A. A. Fresh Look at the Mystery of Magnetization Reversal in YVO_3 . *Inorg. Chem.* **2013**, 52, 8529-8539.
- (34) Belik, A. A. Solid Solutions Between BiMnO_3 and BiCrO_3 . *Inorg. Chem.* **2016**, 55, 12348-12356.
- (35) Belik, A. A.; Glazkova, Y. S.; Terada, N.; Matsushita, Y.; Sobolev, A. V.; Presniakov, I. A.; Tsujii, N.; Nimori, S.; Takehana, K.; Imanaka, Y. Spin-Driven Multiferroic Properties of $\text{PbMn}_7\text{O}_{12}$ Perovskite. *Inorg. Chem.* **2016**, 55, 6169-6177.
- (36) Terada, N.; Glazkova, Y. S.; Belik, A. A. Differentiation Between Ferroelectricity and Thermally Stimulated Current in Pyrocurrent Measurements of Multiferroic $\text{MMn}_7\text{O}_{12}$ ($M = \text{Ca}, \text{Sr}, \text{Cd}, \text{Pb}$). *Phys. Rev. B: Condens. Matter Mater. Phys.* **2016**, 93, 155127.
- (37) De, C.; Ghara, S.; Sundaresan, A. Effect of Internal Electric Field on Ferroelectric Polarization in Multiferroic TbMnO_3 . *Solid State Comm.* **2015**, 205, 61-65.
- (38) Ngo, T. N. M.; Adem, U.; Palstra, T. T. M. The Origin of Thermally Stimulated Depolarization Currents in Multiferroic CuCrO_2 . *Appl. Phys. Lett.* **2015**, 106, 152904.

Table 1. Lattice Parameters (a , b , c , and β) and Unit Cell Volume of $\text{RMn}_7\text{O}_{12}$ ($\text{R} = \text{Sm}$, Eu , and Gd) and $\text{Tb}_{1-\delta}\text{Mn}_7\text{O}_{12-1.5\delta}$ ($\delta = 0, 0.1$, and 0.2) at Room Temperature in Space Group $I2/m$

R	a (Å)	b (Å)	c (Å)	β (deg)	V (Å ³)
Sm	7.4908(1)	7.3522(1)	7.4863(1)	91.211(1)	412.20(2)
Eu	7.4821(1)	7.3471(1)	7.4763(1)	91.192(1)	410.89(2)
Gd	7.4750(2)	7.3441(1)	7.4705(2)	91.200(1)	410.02(2)
Tb	7.4616(1)	7.3441(1)	7.4558(1)	91.121(1)	408.49(1)
Tb _{0.9}	7.4531(2)	7.3497(1)	7.4481(2)	91.073(1)	407.92(2)
Tb _{0.8}	7.4491(2)	7.3496(1)	7.4459(2)	91.063(1)	407.58(2)

Lattice parameters were refined from laboratory XRPD data.

Table 2. Structure Parameters of $(\text{Tb}_{0.88}\text{Mn}_{0.12})\text{Mn}_7\text{O}_{12}$ at 295 K from Synchrotron X-ray Powder Diffraction Data

Site	x	y	z	B (Å ²)
Tb/Mn	0	0	0	0.93(2)
Mn1	0	0.5	0	0.64(4)
Mn2	0.5	0	0	0.41(8)
Mn3	0.5	0.5	0	0.72(9)
Mn4	0.25	0.25	0.25	0.18(3)
Mn5	0.25	0.25	0.75	0.25(3)
O1	0.1590(8)	0	0.3025(8)	0.50(13)
O2	0.1756(8)	0	0.6824(8)	0.28(11)
O3	0.0151(5)	0.3083(6)	0.1724(6)	0.60(12)
O4	0.3109(5)	0.1704(7)	-0.0085(6)	0.48(12)

Crystal data: Space group $I2/m$ (No. 12, unique axis b , cell choice 3), $Z = 2$. $a = 7.44454(2)$ Å, $b = 7.34703(2)$ Å, $c = 7.44215(2)$ Å, $\beta = 91.0621(1)^\circ$, and $V = 406.9807(13)$ Å³; $R_{\text{wp}} = 4.52\%$, $R_{\text{p}} = 2.65\%$, $R_{\text{B}} = 4.97\%$, and $R_{\text{F}} = 3.50\%$. $\rho_{\text{cal}} = 5.902$ g/cm³. The occupation (g) of the Tb/Mn site is $g(\text{Tb}) = 0.883(3)$ and $g(\text{Mn}) = 0.117$. $g = 1$ for all other sites.

The sample had the total chemical composition of $\text{Tb}_{0.8}\text{Mn}_7\text{O}_{11.70}$; and the weight fraction of Mn_2O_3 impurity is 3.9 %.

Table 3. Structure Parameters of SmMn₇O₁₂ and EuMn₇O₁₂ at 100 K from Neutron Powder Diffraction Data

	SmMn ₇ O ₁₂	EuMn ₇ O ₁₂
a (Å)	7.4854(2)	7.4769(3)
b (Å)	7.3287(2)	7.3246(2)
c (Å)	7.4837(2)	7.4748(2)
β (deg)	91.231(2)	91.215(2)
V (Å ³)	410.45(2)	409.27(2)
O1		
x	0.1651(8)	0.1632(8)
z	0.3055(7)	0.3034(7)
O2		
x	0.1781(8)	0.1779(10)
z	0.6850(10)	0.6872(10)
O3		
x	0.0153(6)	0.0146(7)
y	0.3065(6)	0.3054(6)
z	0.1737(6)	0.1743(6)
O4		
x	0.3107(6)	0.3097(6)
y	0.1749(6)	0.1739(6)
z	-0.0123(5)	-0.0124(6)
R (%)	3.4	3.3
wR (%)	3.5	3.2
R(Bragg) (%)	4.9	6.1

Crystal data: Space group: $I2/m$ (unique axis b , cell choice 3); $Z = 2$.

Fractional coordinates: Sm and Eu: $2a$ (0, 0, 0), Mn1: $2b$ (0, 0.5, 0), Mn2: $2c$ (0.5, 0, 0), Mn3: $2d$ (0.5, 0.5, 0), Mn4: $4e$ (0.25, 0.25, 0.25), Mn5: $4f$ (0.25, 0.25, 0.75), O1 and O2: $4i$ (x , 0, z), O3 and O4: $8j$ (x , y , z). $g = 1$ for all sites.

Table 4. Bond Lengths (in Å), Bond-Valence Sum (BVS), Distortion Parameters of MnO₆ Octahedra (Δ), and Mn-O-Mn Bond Angles (deg) in SmMn₇O₁₂ and EuMn₇O₁₂ at 100 K and (Tb_{0.88}Mn_{0.12})Mn₇O₁₂ at 295 K

	SmMn ₇ O ₁₂	EuMn ₇ O ₁₂	(Tb _{0.88} Mn _{0.12})Mn ₇ O ₁₂
R – O1 (x2)	2.575(5)	2.552(5)	2.524(6)
R – O2 (x2)	2.733(7)	2.714(8)	2.723(7)
R – O3 (x4)	2.597(4)	2.590(4)	2.604(4)
R – O4 (x4)	2.659(4)	2.646(4)	2.633(4)
BVS(R ³⁺)	2.75	2.76	2.59
Mn1 – O3 (x4)	1.925(4)	1.933(4)	1.907(4)
Mn1 – O1 (x2)	2.872(6)	2.889(6)	2.910(6)
Mn1 – O2 (x2)	2.805(6)	2.811(8)	2.792(6)
BVS(Mn1 ³⁺)	2.78	2.72	2.90
Mn2 – O4 (x4)	1.911(4)	1.910(4)	1.884(5)
Mn2 – O3 (x4)	2.828(4)	2.825(4)	2.820(4)
BVS(Mn2 ³⁺)	2.88	2.89	3.09
Mn3 – O1 (x2)	1.930(6)	1.930(6)	1.904(5)
Mn3 – O2 (x2)	1.901(7)	1.910(7)	1.867(5)
Mn3 – O4 (x4)	2.773(4)	2.781(4)	2.801(4)
BVS(Mn3 ³⁺)	2.89	2.85	3.09
Mn4 – O1 (x2)	1.986(2)	1.986(2)	1.999(2)
Mn4 – O3 (x2)	1.882(4)	1.882(5)	1.881(4)
Mn4 – O4 (x2)	2.098(4)	2.096(4)	2.069(5)
BVS(Mn4 ³⁺)	3.33	3.33	3.36
Δ(Mn4)	19.7×10 ⁻⁴	19.3×10 ⁻⁴	15.3×10 ⁻⁴
Mn5 – O2 (x2)	1.968(2)	1.963(3)	1.981(2)
Mn5 – O3 (x2)	2.119(5)	2.109(5)	2.111(4)
Mn5 – O4 (x2)	1.908(4)	1.905(4)	1.936(5)
BVS(Mn5 ³⁺)	3.24	3.29	3.12
Δ(Mn5)	19.7×10 ⁻⁴	18.6×10 ⁻⁴	13.6×10 ⁻⁴
Mn4 – O1 – Mn4 (x2)	134.59(9)	134.43(9)	133.55(9)
Mn5 – O2 – Mn5 (x2)	137.2(1)	137.8(1)	136.03(9)
Mn4 – O4 – Mn5 (x2)	138.1(2)	138.1(2)	136.59(9)
Mn5 – O3 – Mn4 (x2)	138.6(2)	139.0(2)	137.61(9)

$BVS = \sum_{i=1}^N \nu_i$, $\nu_i = \exp[(R_0 - l_i)/B]$, N is the coordination number, $B = 0.37$, $R_0(\text{Sm}^{3+}) = 2.088$, $R_0(\text{Eu}^{3+}) = 2.076$, $R_0(\text{Tb}^{3+}) = 2.049$, and $R_0(\text{Mn}^{3+}) = 1.76$.²³

$\Delta = (1/N) \sum_{i=1}^N [(l_i - l_{av})/l_{av}]^2$, where $l_{av} = (1/N) \sum_{i=1}^N l_i$ is the average Mn-O distance and N is the coordination number.

Table 5. Temperatures of Magnetic Anomalies, Parameters of the Curie-Weiss Fits and M vs H curves at 5 K of $\text{RMn}_7\text{O}_{12}$ ($\text{R} = \text{Sm}, \text{Eu}, \text{and Gd}$) and $\text{Tb}_{1-\delta}\text{Mn}_7\text{O}_{12-1.5\delta}$ ($\delta = 0, 0.1, \text{and } 0.2$)

R	T_{N1} (K)	μ_{eff} ($\mu_{\text{B}}/\text{f.u.}$)	μ_{calc} ($\mu_{\text{B}}/\text{f.u.}$)	θ (K)	M_{S} ($\mu_{\text{B}}/\text{f.u.}$)	M_{R} ($\mu_{\text{B}}/\text{f.u.}$)	H_{C} (kOe)
Sm	87	13.790(18)	13.002	-110.2(1.1)	3.47	1.28	~8.8
Eu	87	13.867(11)	13.400	-93.0(6)	4.23	1.51	~4.5
Gd	86	15.373(13)	15.232	-58.2(6)	10.38	2.05	~1.3
Tb	82	15.963(8)	16.070	-36.2(4)	9.60	2.06	~2.0
$\text{Tb}_{0.9}$	77	15.948(13)	15.787	-40.7(5)	9.00	1.81	~2.5
$\text{Tb}_{0.8}$	75	15.709(11)	15.498	-53.2(5)	8.16	1.64	~3.0

The Curie-Weiss fits are performed between 200 and 395 K for the FCC data at 70 kOe. M_{S} is the magnetization value at 5 K and 70 kOe; M_{R} is the remnant magnetization at 5 K, and H_{C} is the coercive field at 5 K. μ_{calc} is calculated using $1.5\mu_{\text{B}}$ for Sm^{3+} , $3.4\mu_{\text{B}}$ for Eu^{3+} , $8\mu_{\text{B}}$ for Gd^{3+} , and $9.5\mu_{\text{B}}$ for Tb^{3+} .²⁹

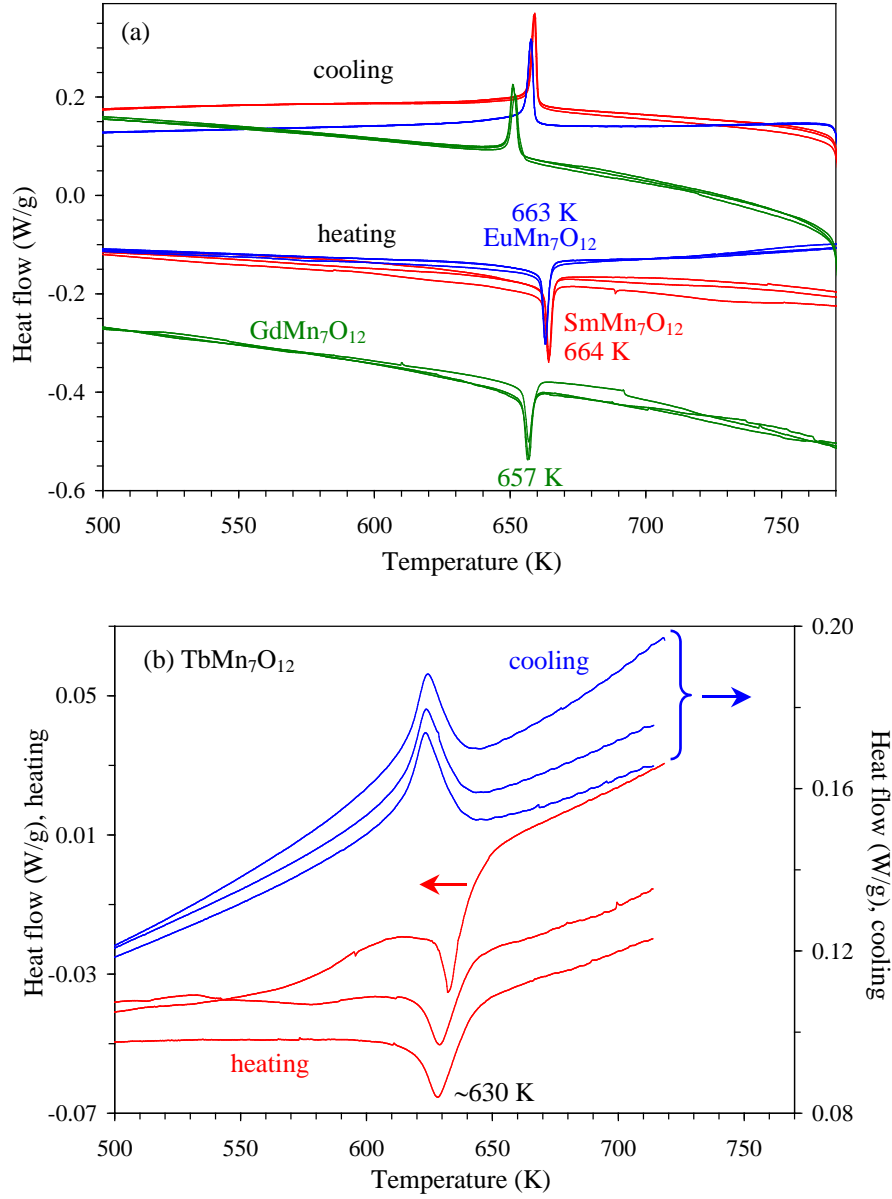


Figure 1. Differential scanning calorimetry (DSC) curves of (a) $\text{SmMn}_7\text{O}_{12}$, $\text{EuMn}_7\text{O}_{12}$, and $\text{GdMn}_7\text{O}_{12}$ and (b) $\text{TbMn}_7\text{O}_{12}$ on heating and cooling (three runs were performed to check the reproducibility; all three runs are shown). Fragments between 500 and 770 K are shown.

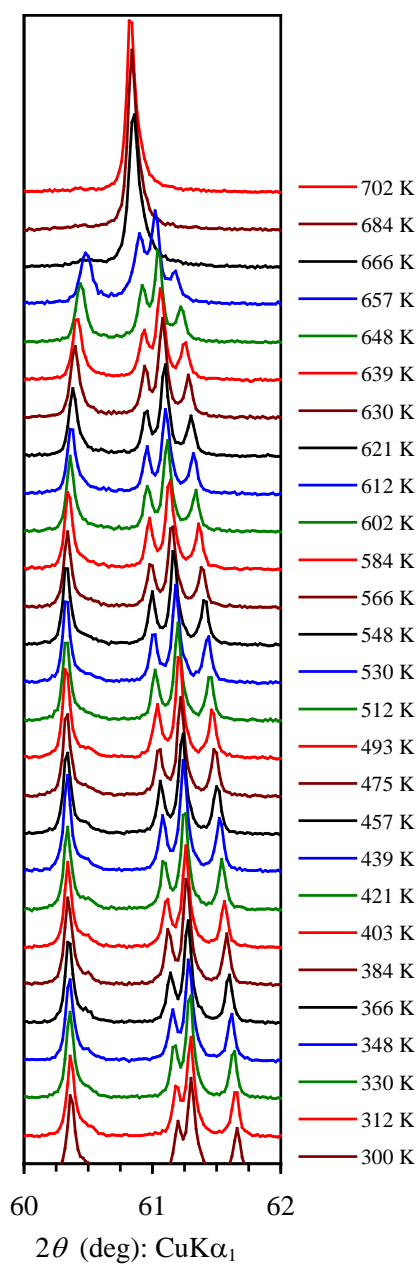


Figure 2. A fragment of high-temperature laboratory X-ray powder diffraction patterns of $\text{GdMn}_7\text{O}_{12}$ showing a phase transition from $I2/m$ to $Im-3$ near 657 K.

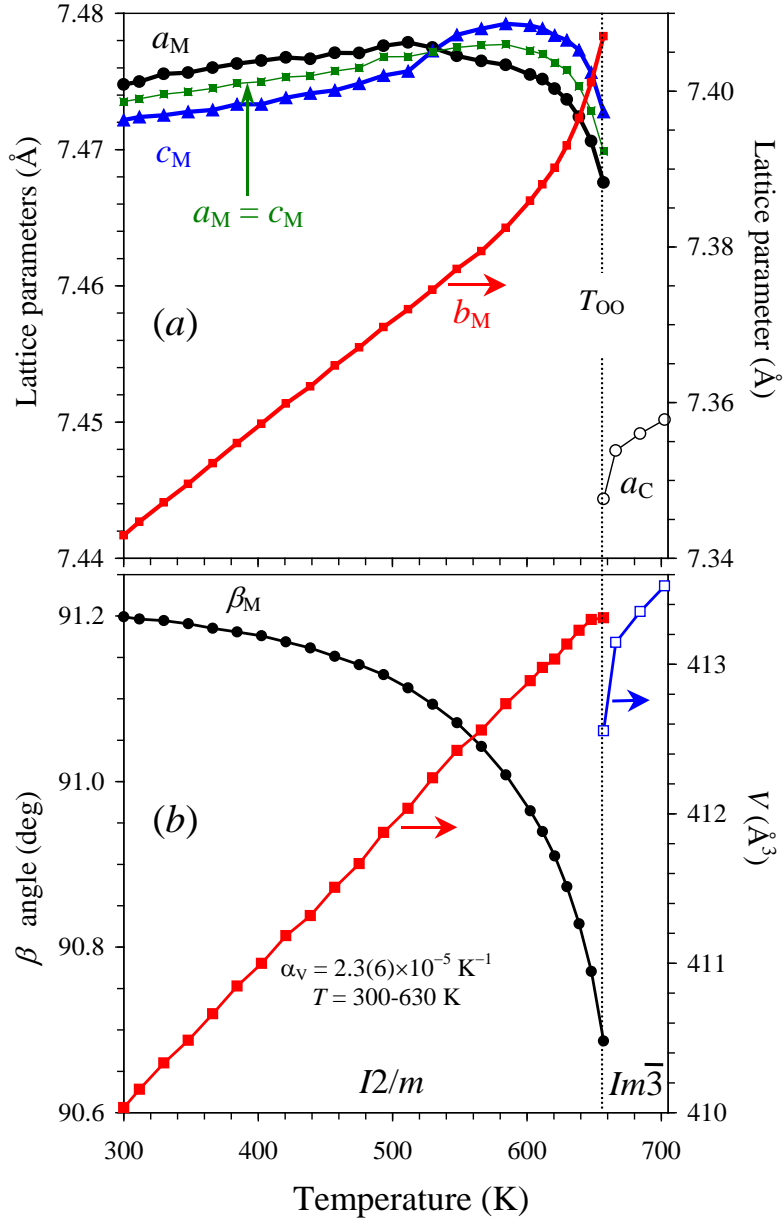


Figure 3. Temperature dependence of (a) the lattice parameters and (b) monoclinic β angle (the left-hand axis) and unit-cell volume (the right-hand axis) of $\text{GdMn}_7\text{O}_{12}$. M: monoclinic, C: cubic, α_V : the volumetric coefficient of thermal expansion. The refinement results with $a_M = c_M$ are shown by green squares, and changes of other parameters are indistinguishable.

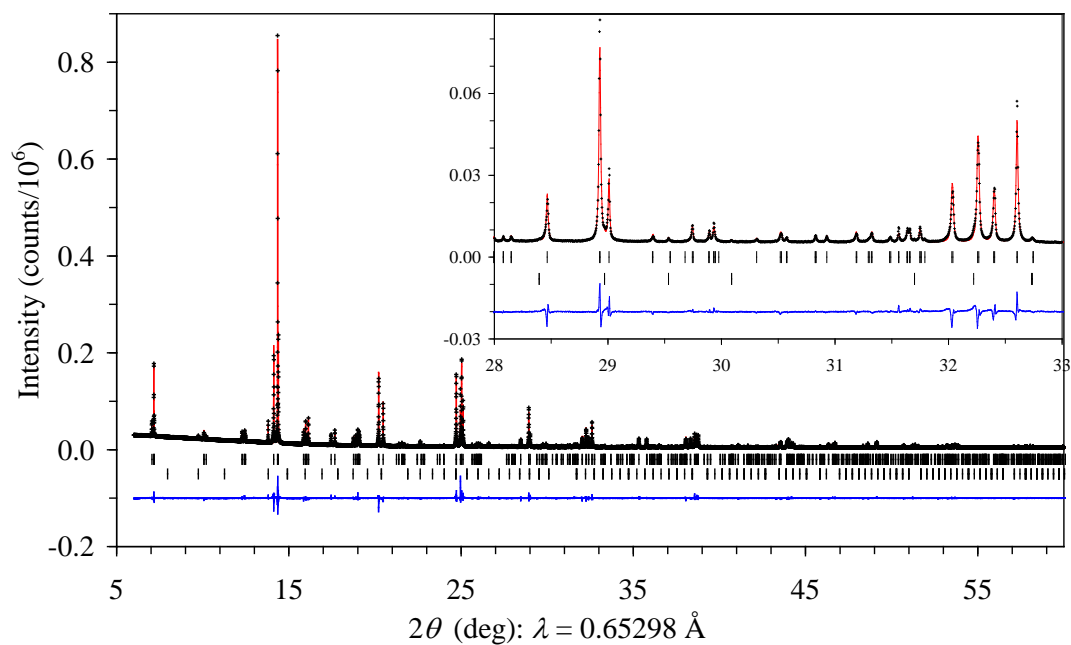


Figure 4. Experimental (black crosses), calculated (red line), and difference (blue line) synchrotron XRPD patterns of the sample with the total chemical composition of $\text{Tb}_{0.8}\text{Mn}_7\text{O}_{11.70}$ at $T = 295 \text{ K}$. The tick marks show possible Bragg reflection positions for $(\text{Tb}_{0.88}\text{Mn}_{0.12})\text{Mn}_7\text{O}_{12}$ (the first row) and Mn_2O_3 impurity (the second row). The inset shows an enlarged fragment.

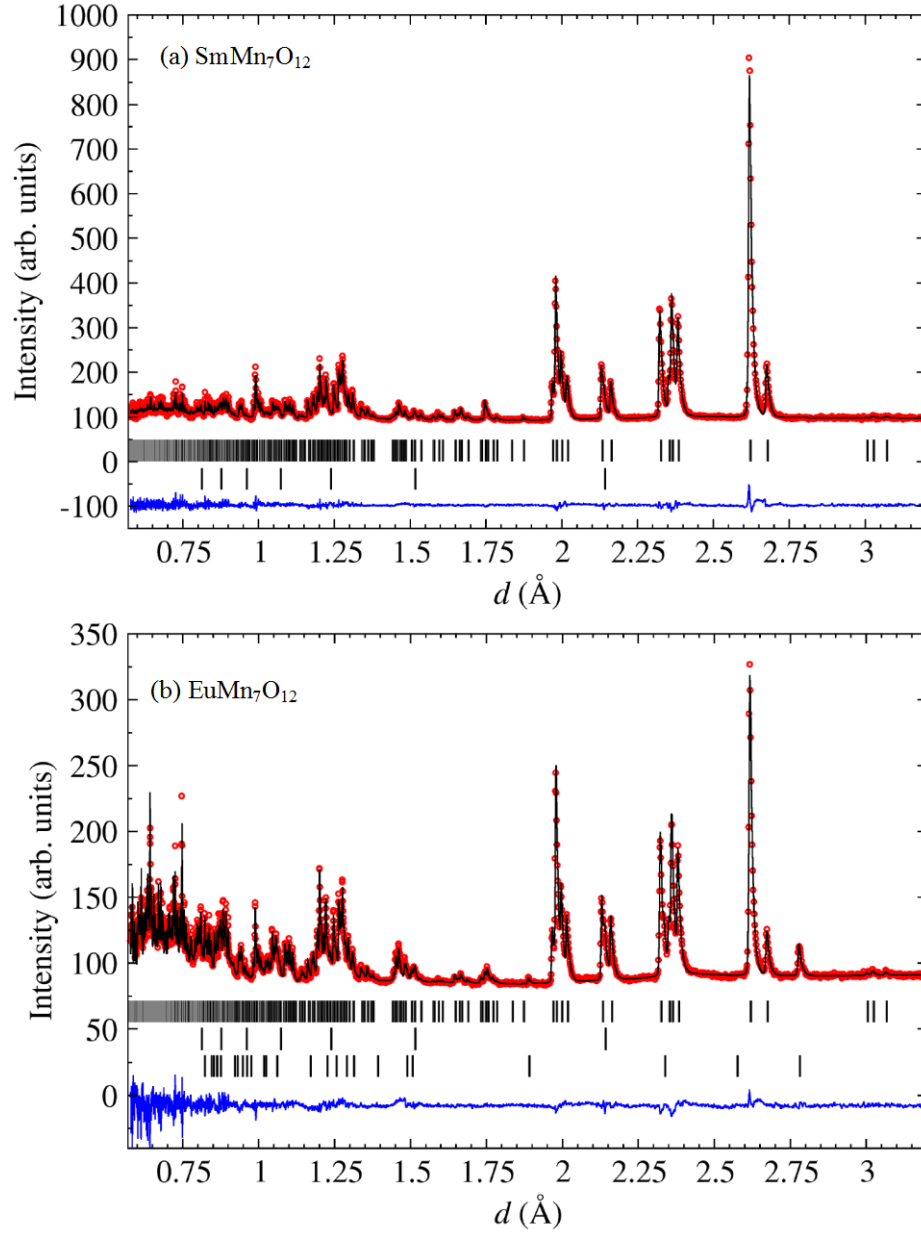


Figure 5. Experimental (red dots), calculated (black lines), and difference (blue lines) neutron powder diffraction patterns at $T = 100$ K for (a) $\text{SmMn}_7\text{O}_{12}$ and (b) $\text{EuMn}_7\text{O}_{12}$. The first row of tick marks corresponds to possible Bragg reflection positions for the perovskite phases. Contributions from vanadium cans are shown by the second row, the third row in panel (b) corresponds to scattering from a Cd mask positioned close to the sample.

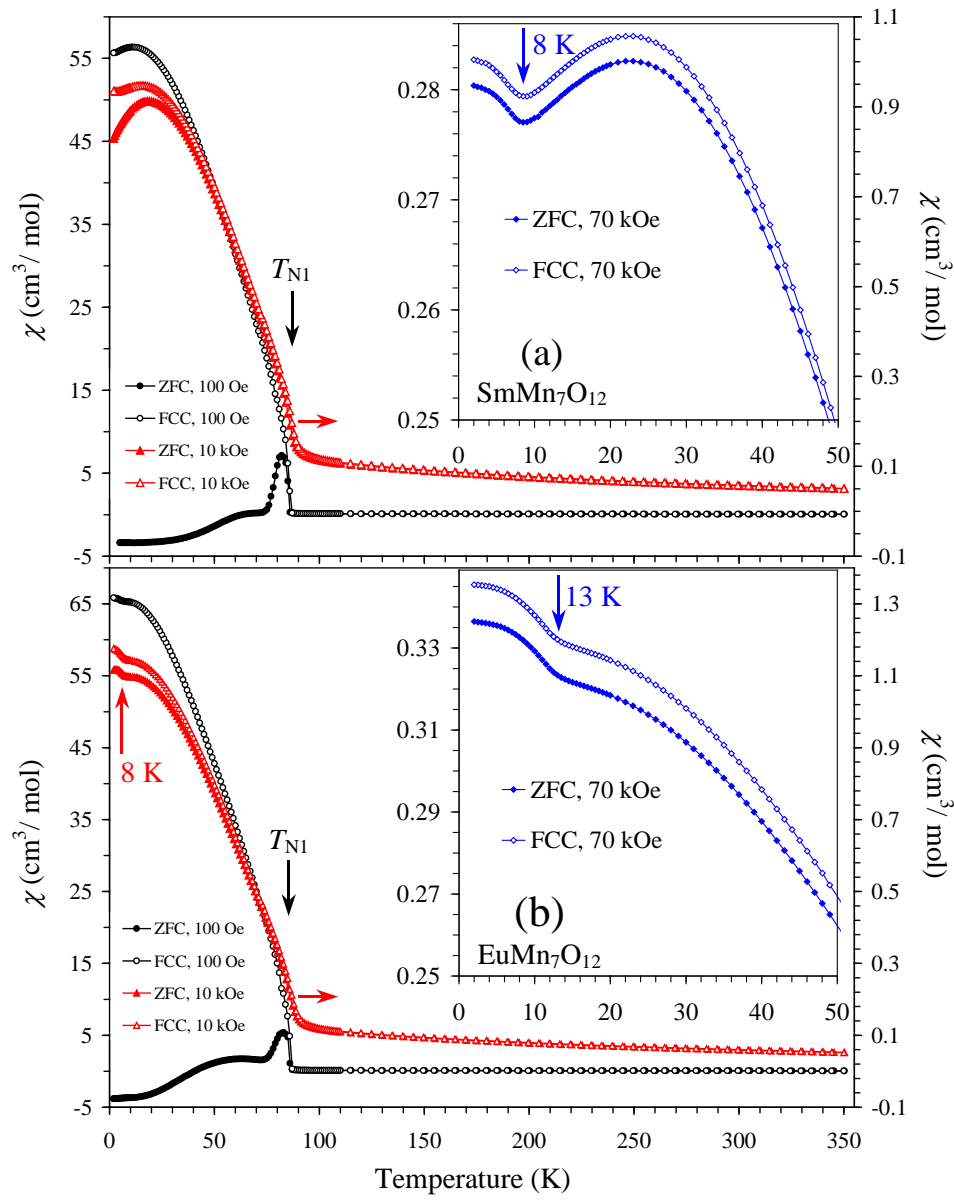


Figure 6. ZFC (filled symbols) and FCC (empty symbols) dc magnetic susceptibility ($\chi = M/H$) curves of (a) $\text{SmMn}_7\text{O}_{12}$ and (b) $\text{EuMn}_7\text{O}_{12}$ at $H = 100$ Oe (left-hand axes) and 10 kOe (right-hand axes). The insets show fragments of the ZFC and FCC χ vs T curves at $H = 70$ kOe.

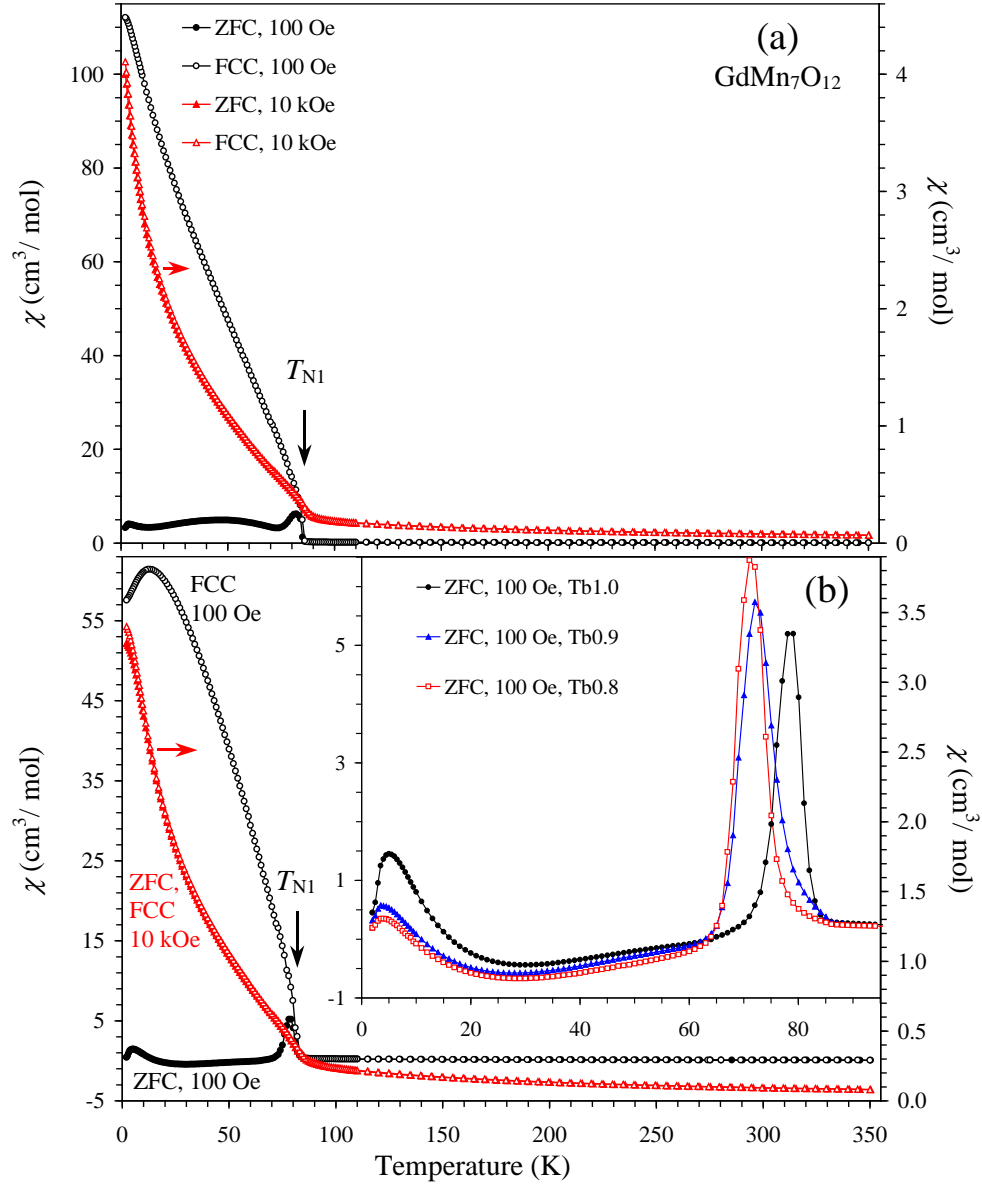


Figure 7. ZFC (filled symbols) and FCC (empty symbols) dc magnetic susceptibility ($\chi = M/H$) curves of (a) $\text{GdMn}_7\text{O}_{12}$ and (b) $\text{TbMn}_7\text{O}_{12}$ at $H = 100$ Oe (left-hand axes) and 10 kOe (right-hand axes). The inset shows the ZFC (\equiv q-ZFC) curves of $\text{TbMn}_7\text{O}_{12}$, $\text{Tb}_{0.9}\text{Mn}_7\text{O}_{11.85}$, and $\text{Tb}_{0.8}\text{Mn}_7\text{O}_{11.70}$ at $H = 100$ Oe.

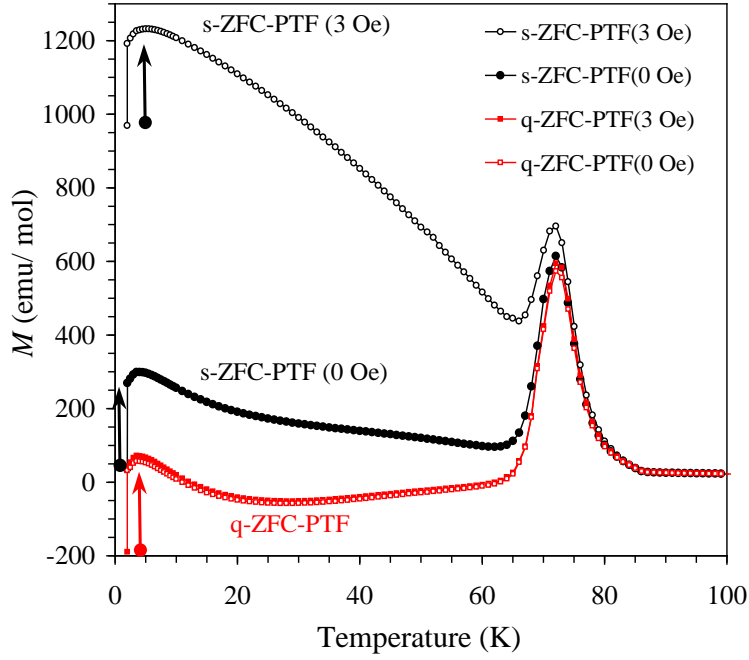


Figure 8. ZFC M versus T curves of $\text{Tb}_{0.9}\text{Mn}_7\text{O}_{11.85}$ at $H = 100$ Oe measured in different procedures: q-ZFC and s-ZFC (see the text). PTF: a positive trapped field. The first point at 2 K is the magnetization value in nominal zero magnetic fields (after inserting the sample into a magnetometer). Arrows show the change of magnetization after the application of the measurement magnetic field of 100 Oe.

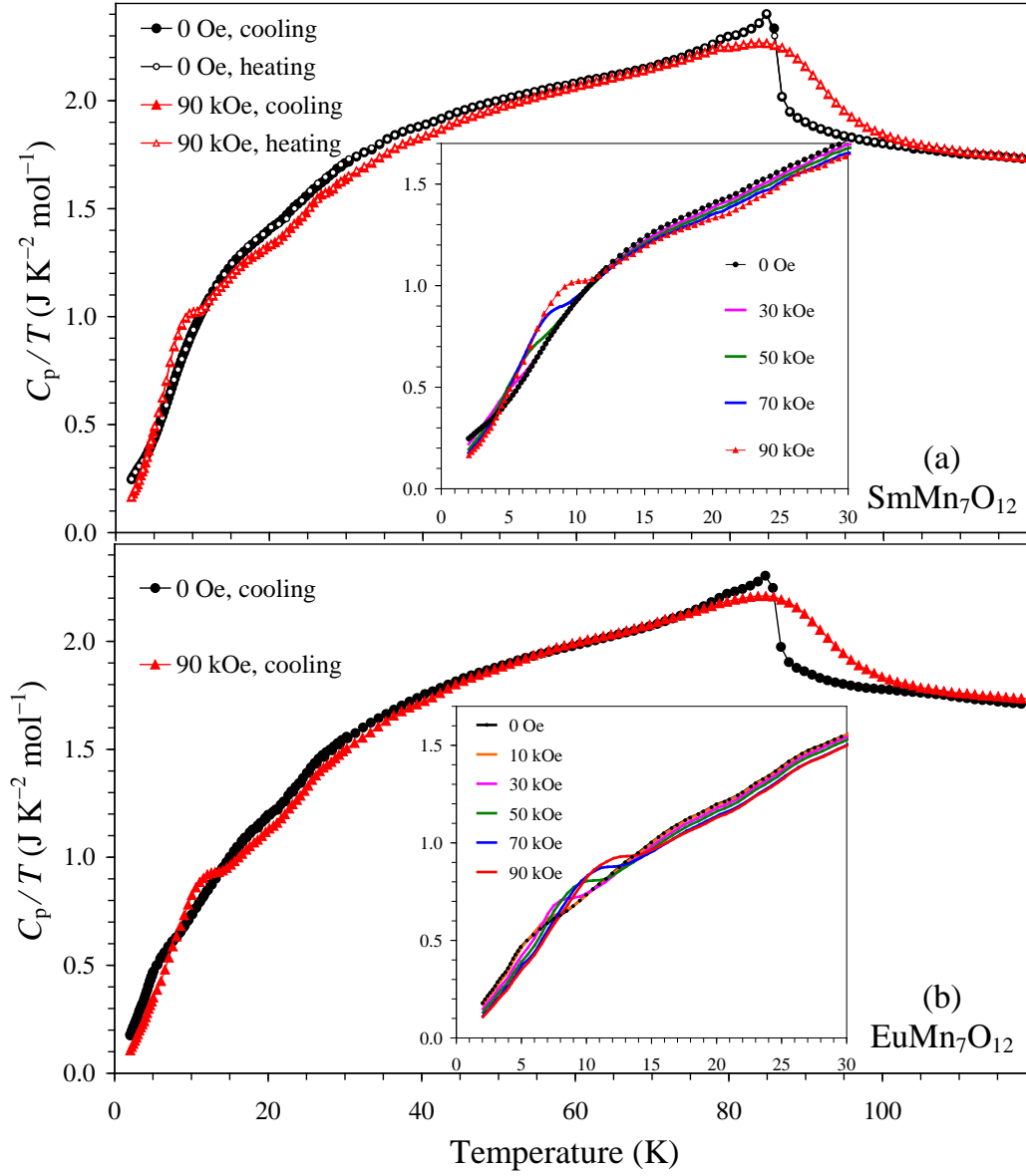


Figure 9. Specific heat of (a) $\text{SmMn}_7\text{O}_{12}$ and (b) $\text{EuMn}_7\text{O}_{12}$ at $H = 0$ and 90 kOe plotted as C_p/T versus T . Measurements were performed on cooling and heating for $\text{SmMn}_7\text{O}_{12}$, and no hysteresis was observed. The insets show C_p/T versus T curves below 30 K at different magnetic fields (measured on cooling). Small depression near 22 K is an instrumental artifact.

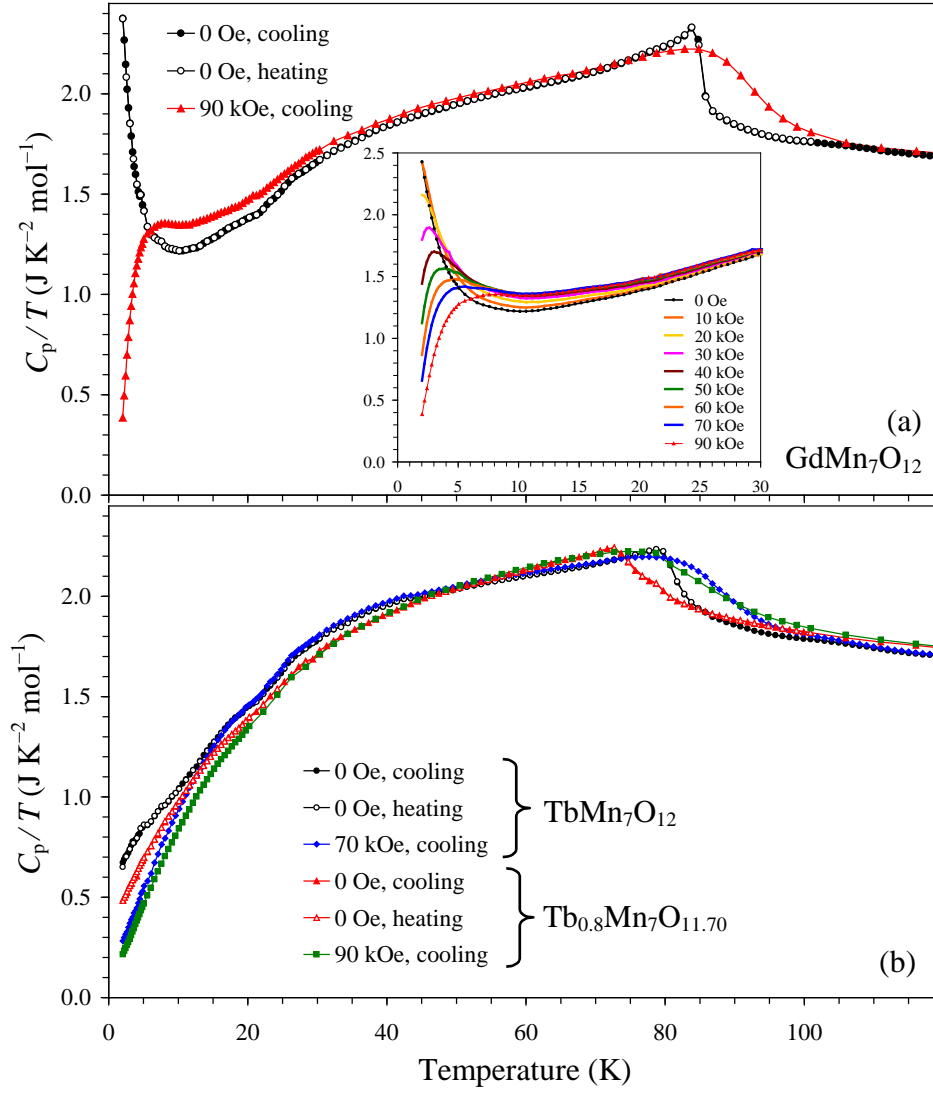


Figure 10. Specific heat, plotted as C_p/T versus T , of (a) $\text{GdMn}_7\text{O}_{12}$ at $H = 0$ and 90 kOe and (b) $\text{TbMn}_7\text{O}_{12}$ at $H = 0$ and 70 kOe and $\text{Tb}_{0.8}\text{Mn}_7\text{O}_{11.70}$ at $H = 0$ and 90 kOe. Measurements were performed on cooling and heating at $H = 0$ Oe, and no hysteresis was observed. The inset shows C_p/T versus T curves below 30 K at different magnetic fields (measured on cooling) for $\text{GdMn}_7\text{O}_{12}$.

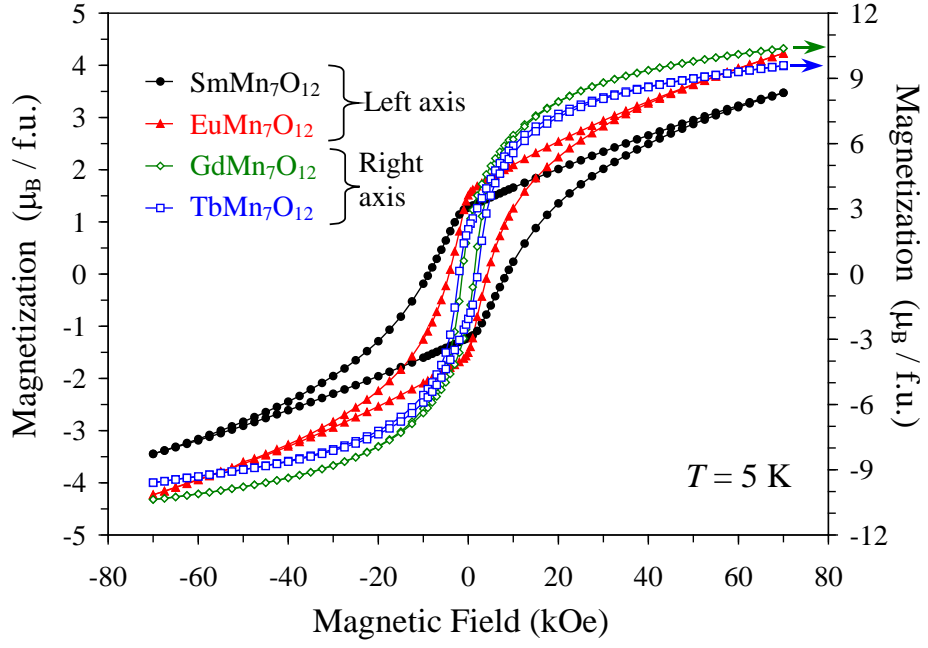


Figure 11. M versus H curves at $T = 5$ K for $\text{SmMn}_7\text{O}_{12}$ and $\text{EuMn}_7\text{O}_{12}$ (the left-hand axis) and for $\text{GdMn}_7\text{O}_{12}$ and $\text{TbMn}_7\text{O}_{12}$ (the right-hand axis). f.u.: formula unit.

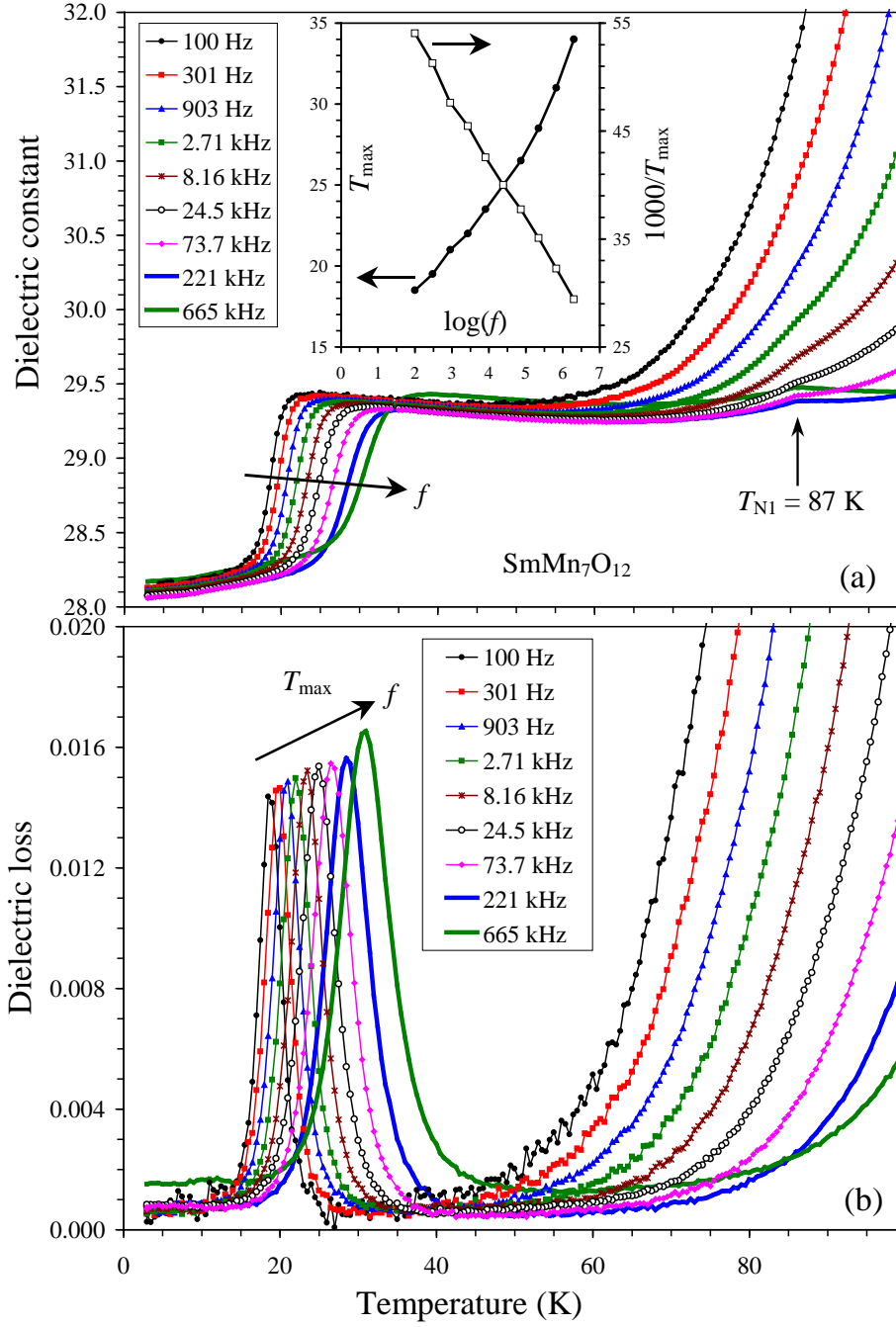


Figure 12. (a) Dielectric constant and (b) dielectric loss of $\text{SmMn}_7\text{O}_{12}$ as functions of temperature. Measurements were performed on cooling at zero magnetic field at different frequencies. The inset shows T_{\max} versus $\log(f)$ and $1000/T_{\max}$ versus $\log(f)$ curves, where T_{\max} is the temperature peak position on dielectric loss.

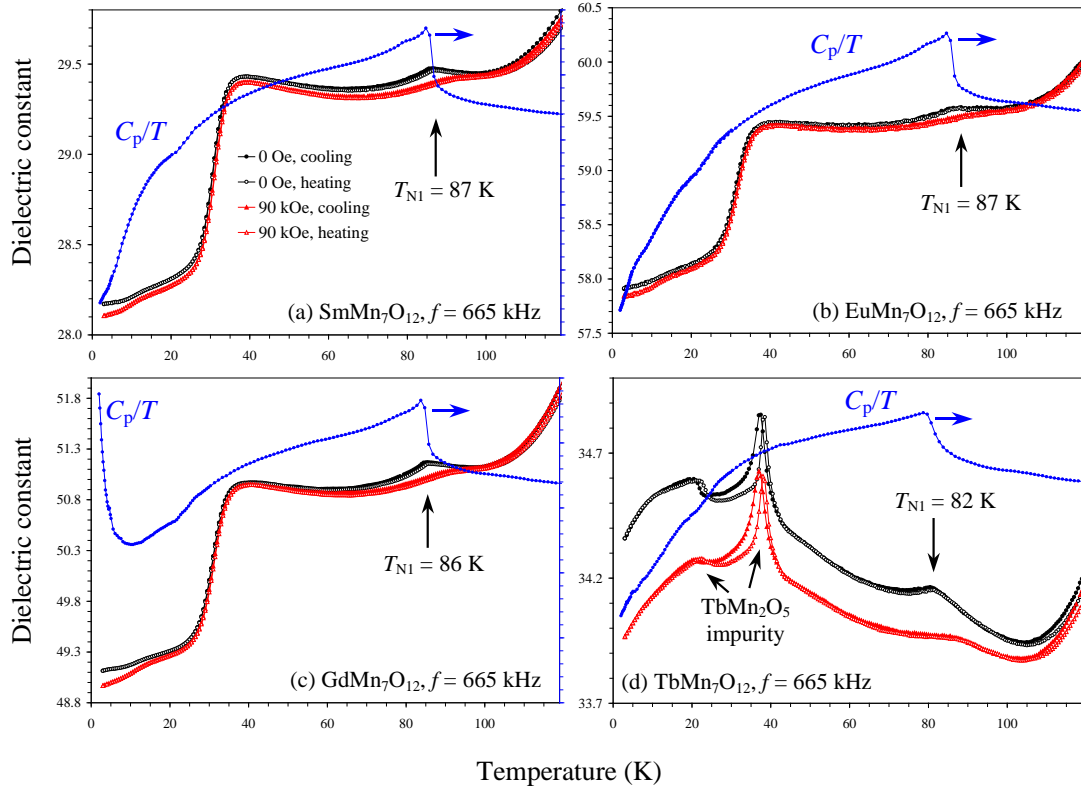


Figure 13. Temperature dependence of dielectric constant in (a) $\text{SmMn}_7\text{O}_{12}$, (b) $\text{EuMn}_7\text{O}_{12}$, (c) $\text{GdMn}_7\text{O}_{12}$, and (d) $\text{TbMn}_7\text{O}_{12}$. Measurements were performed on cooling (filled symbols) and heating (empty symbols) at $H = 0$ Oe (black curves) and 90 kOe (red curves). Curves at one frequency of 665 kHz are shown. The right-hand axes give C_p/T versus T curves measured at $H = 0$ Oe on cooling (the scale is from 0 to 2.5 $\text{JK}^{-2}\text{mol}^{-1}$).

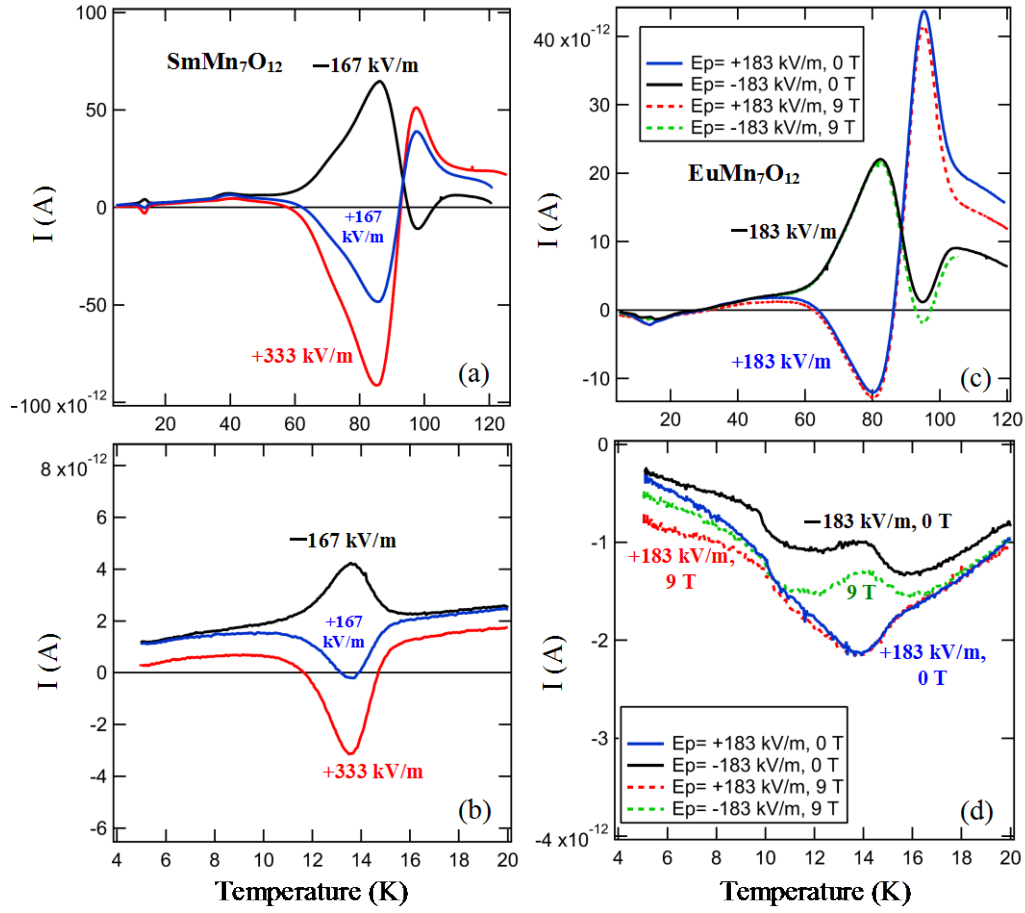


Figure 14. (a, b) Results of pyroelectric current measurements for $\text{SmMn}_7\text{O}_{12}$ at zero magnetic field. The poling was performed from 100 K to 5 K under the poling fields $E_p = +167$, $+333$, and -167 kV/m. The panel (b) shows details of measurements below 20 K. (c, d) Results of pyroelectric current measurements for $\text{EuMn}_7\text{O}_{12}$. The poling was performed from 100 K to 5 K under the poling fields $E_p = +183$ and -183 kV/m and under $H = 0$ Oe (0 T) and 90 kOe (9 T). The panel (d) shows details of measurements below 20 K.

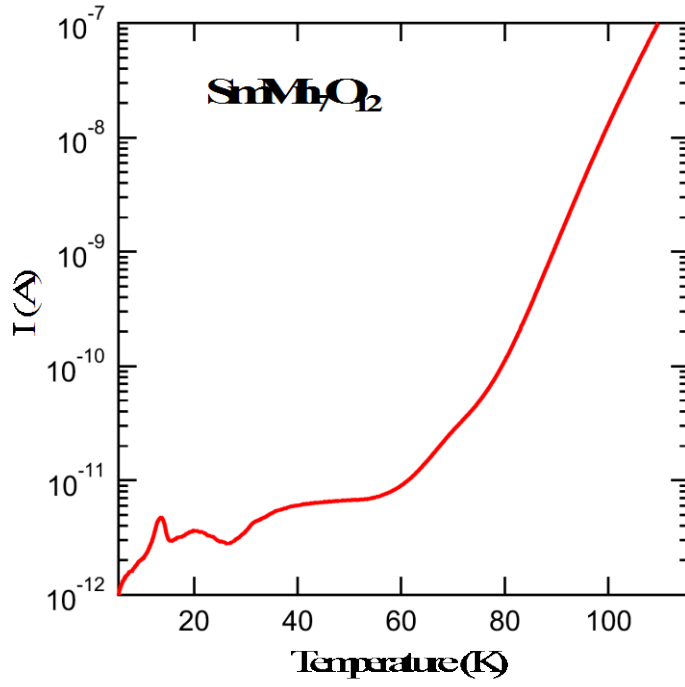


Figure 15. Variations of the electric current in $\text{SmMn}_7\text{O}_{12}$ on heating under a bias electric field of +167 kV/m. After cooling to 5 K under zero electric field, electric current was measured under the bias electric field on heating.